THESIS FOR THE DEGREE OF DOCTOR OF PHILOSOPHY

Quantum Materials Probed by Light and Electron Spectroscopy

KARIN MARIA VON ARX

UNIVERSITAS TURICENSIS
MDCCCXXXIII

Department of Physics
CHALMERS UNIVERSITY OF TECHNOLOGY
Gothenburg, Sweden 2023

Quantum Materials Probed by Light and Electron Spectroscopy
KARIN MARIA VON ARX
ISBN 978-91-7905-938-5

Doktorsavhandlingar vid Chalmers tekniska högskola
Ny serie nr 5404
ISSN 0346-718X

Department of Physics
Chalmers University of Technology
SE-412 96 Gothenburg
Sweden
Telephone + 46 (0)31-772 1000

Cover: Illustration of a PhD phase diagram

This thesis is for a double degree at Chalmers University of Technology and University of Zurich.

Chalmers, Chalmers digitaltryck
Gothenburg, Sweden 2023

Quantum Materials Probed by Light and Electron Spectroscopy

Dissertation

zur

Erlangung der naturwissenschaftlichen Doktorwürde
(Dr. sc. nat.)

vorgelegt der

Mathematisch-naturwissenschaftlichen Fakultät

der

Universität Zürich

von

Karin Maria von Arx

von

Egerkingen SO

Promotionskommission

Prof. Dr. Johan Chang (Vorsitz)

Prof. Dr. Yasmine Sassa

Prof. Dr. Fabian Natterer

Prof. Dr. Elizabeth Blackburn

Zürich, 2023

Abstract

Since new technologies depend heavily on material properties, the quest for novel tunable electronic and magnetic materials occupies a large part of current research efforts. Especially promising are quantum materials, which exhibit a wide range of exotic electronic and magnetic phenomena, and which often show a great sensitivity to external perturbations such as temperature and pressure changes and chemical doping. At the origin of many of these phenomena lie strong many-body correlations and competition between different energy scales, from which rich phase diagrams with a variety of structural, electronic and magnetic phases emerge. Understanding the microscopic processes in these materials relies on the knowledge of the relevant correlations and is one of the most important efforts in the field of condensed matter physics.

This thesis focuses on three types of quantum materials that exhibit strong correlations and an unconventional superconducting phase. An experimental study investigates the electronic correlations in phases close to superconductivity, providing insight into energy scales that define the electronic ground state.

The first material family is the calcium ruthenates, an archetypal system for the study of spin–orbit coupling effects and the Mott metal–insulator transition. The competition of different energy scales leads to a non-trivial ground state, from which a complex excitation spectrum emerges. This work presents a study of the low-energy spin–orbital excitations in the single and bilayer compounds, shedding light on the importance of the coupling between spin and orbital angular momentum.

The second material family is the high-temperature superconducting La-based cuprates. The detailed connections between superconductivity and its surrounding phases remain elusive. The resonant inelastic x-ray scattering study presented here investigates the charge order phase and highlights the importance of an energy resolved technique to study weak charge correlations as a function of temperature and hole doping. The connection between the charge order and the surrounding phases is investigated, and the importance of a momentum-dependent electron–phonon coupling is revealed.

The third material is the spinel oxide superconductor $LiTi_2O_4$. New experimental insights have recently challenged the picture of a conventional s-wave superconductor and provided evidence for an anomalous pairing mechanism. The understanding has been impeded by the lack of direct measurements of the electronic band structure. This work presents an extensive angle-resolved photoemission spectroscopy study, revealing strong correlation effects at a low energy scale.

Keywords: quantum materials, superconductivity, spin–orbit coupling, electron–phonon coupling, RIXS, ARPES

List of Publications

This thesis is based on work contained in the following publications:

1. Resonant inelastic x-ray scattering study of $Ca_3Ru_2O_7$
   K. von Arx, F. Forte, M. Horio, V. Granata, Q. Wang, L. Das, Y. Sassa, R. Fittipaldi, C. G. Fatuzzo, O. Ivashko, Y. Tseng, E. Paris, A. Vecchione, T. Schmitt, M. Cuoco, J. Chang
   Phys. Rev. B 102, 235104 (2020)
   Contribution: I performed all the data analysis and took the lead in manuscript preparation and discussions with theoreticians.

2. Resolving the Orbital Character of Low-energy Excitations in Mott Insulator with Intermediate Spin-orbit Coupling
   K. von Arx, P. Rothenbühler, Qisi Wang, J. Choi, M. Garcia-Fernandez, S. Agrestini, Ke-Jin Zhou, A. Vecchione, R. Fittipaldi, Y. Sassa, M. Cuoco, F. Forte, J. Chang
   Manuscript submitted to npj Quantum Mater., under review (2023)
   Contribution: I planned the experiment and prepared the samples. Together with co-authors, I performed the experiments. I guided and assisted a master's student with the data analysis. I took the lead in manuscript preparation and discussions with theoreticians.

3. High-temperature charge-stripe correlations in $La_{1.675}Eu_{0.2}Sr_{0.125}CuO_4$
   Q. Wang, M. Horio, **K. von Arx**, D. Mukkattukavil, Y. Sassa, S. Pyon, T. Takayama, H. Takagi, Y. Tseng, W. Zhang, T. Schmitt, J. Chang
   Phys. Rev. Lett. 124, 187002 (2020)
   Contribution: I participated in the experiments and contributed to discussions and manuscript preparation.

4. Fate of Charge Order in Overdoped La-Based Cuprates
   K. von Arx, Qisi Wang, S. Mustafi, D. G. Mazzone, M. Horio, D. John Mukkattukavil, E. Pomjakushina, S. Pyon, T. Takayama, H. Takagi, T. Kurosawa, N. Momono, M. Oda, N. B. Brookes, D. Betto, W. Zhang, T. C. Asmara, Y. Tseng, T. Schmitt, Y. Sassa, J. Chang
   npj Quantum Mater. 8, 7 (2023)
   Contribution: I planned, prepared and performed the experiments. I analysed the data and wrote the manuscript with input from co-authors.

5. Charge Order Lock-in by Electron-Phonon Coupling in $La_{1.675}Eu_{0.2}Sr_{0.125}CuO_4$
   Qisi Wang, **K. von Arx**, M. Horio, D. John Mukkattukavil, J. Küspert, Y.

Sassa, T. Schmitt, A. Nag, S. Pyon, T. Takayama, H. Takagi, M. Garcia-Fernandez, Ke-Jin Zhou, J. Chang
Sci. Adv. 7, 27 (2021)
Contribution: I participated in the preparation and execution of the experiments and the data analysis. I contributed to discussions and manuscript preparation.

6. Evidence of strong electron correlations in the spinel superconductor $LiTi_2O_4$
K. von Arx, Y. Ge, M. Hengsberger, O. Forslund, C. Lin, F. Elson, W. Chen, M. Månsson, J. Chang, M. Radovic, A. Chikina, Y. Sassa
Manuscript
Contribution: I planned and took the lead in the execution of the experiments. I analysed the data and wrote the manuscript with inputs from co-authors.

Contents

1 Introduction

Science has its origins in the curiosity of humankind, and this curiosity played a major role in shaping the world we live in. The evolution we undertook as a society was often fuelled by our desire to understand things, make new discoveries and explore our surroundings. This curiosity is therefore the foundation on which new technologies have been developed. Important technological evolutionary steps were often connected to the discovery of a new material and its usage, like iron in the Iron Age or the semiconductor silicon in the recent Silicon/Digital Age. This illustrates how material science is and has always been a central part of our efforts to advance. It is therefore no surprise that material science is still among the largest scientific disciplines, spanning a broad range of fields from battery research to the production of synthetic polymers, known as plastics.

This thesis focuses on fundamental material science within condensed matter physics, which is dedicated to understanding the macroscopic and microscopic properties of condensed matter. This is vital for the development and exploitation of new exotic materials that will form the basis for many new technologies. The general importance of fundamental or basic science has been acknowledged worldwide, with the United Nations General Assembly launching the International Year of Basic Sciences for Sustainable Development in 2022 and 2023 [1]. This international year highlights the essential role of curiosity-based science in the challenges faced by humanity and the implementation of the 17 Sustainable Development Goals (SDGs). The technological innovations generated by fundamental sciences can contribute to the SDGs by providing new means for global energy, water and food access as well as communication technologies. Material science, which looks deeply into the properties and mechanisms of materials, is an important part of this endeavour towards a more sustainable future.

Materials exhibiting interesting electronic and magnetic properties are built as crystalline lattices, in which a base consisting of one or more elements in a specific arrangement is periodically repeated to form a crystal. A well-known example is sodium chloride, with the chemical formula NaCl, which is nothing more than table salt. Its structure is depicted in Fig. 1.1a, where the elements Na and Cl are schematically drawn as balls and the solid black lines indicate the so-called

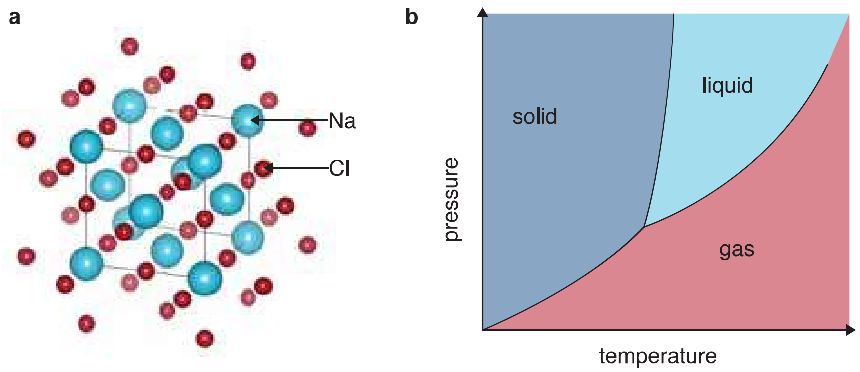

Figure 1.1: Crystalline structure and phase diagram. **a** Crystal structure of NaCl, commonly known as table salt. Solid black lines indicate the unit cell of the lattice. **b** Schematic phase diagram of water as a function of pressure and temperature, showing three phases: solid, liquid and gas.

unit cell, the base that forms the building block of the lattice. To characterize the properties of materials, one depicts the states in which the material can exist, the so-called phases, in phase diagrams. One of the simplest examples is shown in Fig. 1.1b, where the solid, liquid and gas phases are indicated as a function of temperature and pressure. In general, phase diagrams can be drawn as functions of different control parameters, like temperature, pressure, magnetic field strength or chemical substitution/doping. Examples of phase transitions range from boiling or freezing of liquids to magnetic transitions, like the Curie temperature, above which the magnetization of a ferromagnetic material is zero. The theoretical concept of phase transitions was developed in the field of thermodynamics, and they are linked to transitions from a disordered to an ordered state. The goal of condensed matter physics is the discovery, characterization, understanding and control of states of matter and their properties for future technological applications.

For example, the understanding of semiconductor physics made it possible to develop computers and mobile phones. The electronic properties of a semiconductor can be explained and exploited by applying the Schrödinger equation for the electron wave function, using a Hamiltonian consisting of a kinetic energy term and a crystal potential term. The solutions for a periodic crystal potential are Bloch states with eigenvalues representing the electronic dispersion [2]. This theory had a tremendous success and forms the basis for our understanding of metals, band insulators and semiconductors. However, many exotic phenomena observed in condensed matter cannot be explained by this theory based on the independent electron picture.

1.1 Quantum Materials and Strong Correlations

Beyond the independent electron picture, interactions between electrons themselves, interactions between electrons and the lattice, and magnetic interactions alter the electronic structure and call for a new description. Such interactions lead to complex many-body problems and various collective behaviours, resulting in new emergent phenomena. Among these phenomena are superconductivity, the quantum Hall effect or heavy fermions. Materials exhibiting such behaviour are commonly known as *quantum materials*, or in the case of strong correlations, *strongly correlated electron systems*. A characteristic of quantum materials is a rich phase diagram resulting from different and often competing interactions between the lattice, charge, orbital and spin degrees of freedom. The system is therefore in a rather fragile balance and small perturbations in the form of thermal energy, pressure, a magnetic field or doping can result in a drastic change in the material's properties. The sheer number of constituents and interaction terms in the associated many-body problem presents one of the most difficult challenges in physics but also offers some of the most promising applications. Strong correlations can, for example, result in metal-to-insulator transitions, colossal magnetoresistance or high-temperature superconductivity.

1.1.1 Superconductivity

The most prominent examples of quantum materials are superconductors, since their properties are most fascinating and they offer promising applications. Superconductivity was discovered by Heike Kamerlingh Onnes in 1911, when he measured the resistance of mercury cooled down with liquid helium and observed a sudden drop to the lowest detectable values at a temperature of 4.2 K; see Fig. 1.2a. In fact, the resistivity of superconductors drops to zero at their transition temperature T_C, making them perfect conductors. On top of that, the superconducting phase is also characterized by diamagnetism, which means an expulsion of magnetic field lines, known as the Meissner effect. These two combined effects of superconductivity are remarkable and were beyond the understanding of the time. Since this discovery, an immense amount of effort has been put into the research of superconductors, and many more elements and alloys have been found to exhibit the described phenomena. Despite all the effort, it took scientists almost 50 years to develop a theory explaining the mechanism behind superconductivity. In 1957, Bardeen, Cooper and Schrieffer succeeded with their "microscopic theory of superconductivity", now called the BCS theory after its discoverers, to explain how the electrons in a material condense in so-called Cooper pairs mediated by lattice vibrations called phonons [3]. According to this theory, there is an upper limit on the transition temperature, which was

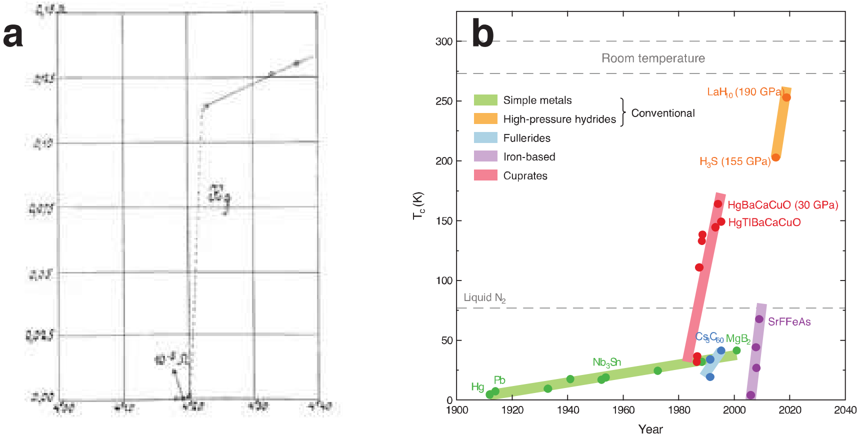

Figure 1.2: Superconductivity. **a** Image of the original figure published by Heike Kamerlingh Onnes showing the resistance of mercury as a function of temperature. From Ref. [6]. **b** Superconductor families as a function of the year of their discovery and their transition temperature T_C. Adapted from Ref. [7].

believed at that time to be around 30 K. This was regarded as a disappointment, since room-temperature superconductors could have revolutionized technology in an unprecedented way. However, as discussed in more detail in chapter 4, the discovery of high-temperature superconductors reignited this dream.

The physics in high-temperature superconductors differs from the BCS theory, and therefore they are referred to as unconventional superconductors, opposed to BCS conventional superconductors. Since their discovery, many more systems have been found to exhibit this unconventional superconductivity, and the race to find the material with the highest transition temperature is still ongoing, as illustrated in Fig. 1.2b. Researchers around the world have put a great deal of effort into the field of high-temperature superconductors, but the detailed mechanisms of these different systems remain unclear. Nevertheless, in recent years, claims of materials exhibiting room-temperature superconductivity at ambient pressure have received significant media coverage. In the most recent example in July 2023, a preprint reported a material called LK-99 to be superconducting at a transition temperature over 400 K and at ambient pressure [4]. However, these findings could not be replicated and the claims were later proven to be false [5]: LK-99 is not a superconductor, but an insulator. Impurities in the material, however, led to a remarkable drop in resistivity. Furthermore, the reported partial levitation did not originate in superconductivity, but in ferromagnetic impurities. Therefore, the search for a room-temperature superconductor, and a full understanding of high-temperature unconventional superconductivity, continues.

Despite the numerous open questions and the need for cooling to low temperatures, superconductivity has already been implemented in a range of applications. High-temperature superconductors that have a transition temperature above the liquid nitrogen level can be used at relatively low costs. One application is in magnetic resonance imaging (MRI) in medicine, in which superconductors are used to generate very strong magnetic fields. Another example is the use of superconducting cables in wind turbines to transport a high current without any losses at a relatively low weight. In addition to the existing applications, room-temperature superconductors promise numerous other advantages, as they could be used in consumer devices, allowing fast charging of electric vehicles, a power grid without any losses, and ideal power storage in the form of never decaying electric loop currents. These applications would facilitate the electrification of society immensely, and could therefore accelerate the transition away from fossil fuels. However, it has to be mentioned that room-temperature superconductivity would not solve all the problems, as some technologies have other limiting factors besides the transition temperature. For example, quantum computers are kept at temperatures close to absolute zero because their performance decreases rapidly when the temperature increases due to noise from thermal vibrations. additionally, when superconductors are used as electromagnets to generate strong magnetic fields, the limiting factor is often the upper critical field or critical current, rather than the transition temperature [8].

1.1.2 Beyond Superconductivity

In addition to the fascination of superconductivity, quantum materials exhibit many other intriguing properties and phases that promise useful applications. Interestingly, unconventional superconductivity is often found in the vicinity of insulating magnetic phases. This is counter-intuitive at first sight, as it is hard to understand how an insulator can become a perfect conductor with only marginal perturbation in the form of pressure or doping. However, several material families exhibit similar phase diagrams with a superconducting dome close to an antiferromagnetic Mott insulating phase. This is illustrated in Fig. 1.3, where schematic phase diagrams for four different unconventional superconductor families are shown: the copper oxide (cuprate) superconductors, the $\mathrm{Ca}_{2-x}\mathrm{Sr}_x\mathrm{RuO}_4$ single-layer system (ruthenate), the heavy fermion superconductors and the iron-based superconductors. By doping or applying pressure to an antiferromagnetic insulator, the system can enter a superconducting state at low temperatures. This suggests that superconductivity emerges from magnetic correlations, or is at least strongly influenced by them. Especially in the cases of copper-based superconductors or the $\mathrm{Ca}_{2-x}\mathrm{Sr}_x\mathrm{RuO}_4$ system shown in panels a and b, superconductivity is surrounded by several other magnetic and electronic phases, indicating the interplay between different interactions leading

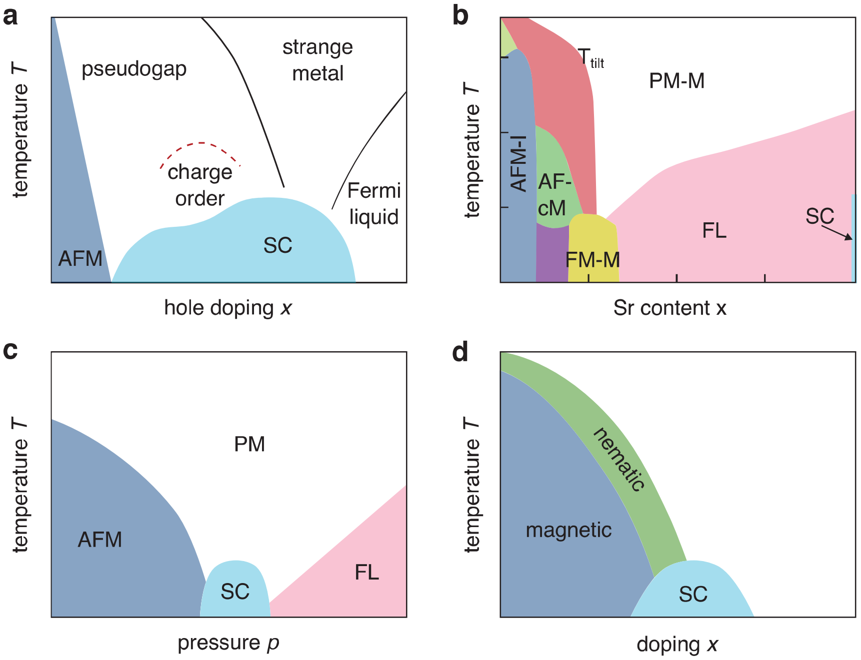

Figure 1.3: Phase diagrams of unconventional superconductors. Schematic phase diagrams for different material families. **a** Copper-based superconductors. Adapted from Ref. [9]. **b** $Ca_{2-x}Sr_xRuO_4$. Adapted from Ref. [10]. **c** Heavy fermion superconductors. Adapted from Ref. [11]. **d** Iron-based superconductors. Adapted from Ref. [12]. Abbreviations for different phases: superconducting (SC), antiferromagnetic (AFM), ferromagnetic (FM), paramagnetic (PM), insulator (I), metal (M), correlated metal (cM), Fermi liquid (FL).

to competing phases.

The interactions between the lattice, charge, orbital and spin degrees of freedom mentioned at the beginning of this section indeed play an important role in the tunability of these materials and the emergence of different phases. To evaluate the microscopic models describing these materials' properties, it is not enough to consider quasi-free electrons in a periodic potential created by the crystal lattice: interactions such as electron–phonon coupling and spin–orbit coupling also have to be taken into account as they alter the electronic band structure significantly. Figure 1.4 illustrates the different elementary degrees of freedom in correlated materials and some of the possible interactions between them. To understand the mechanisms in correlated materials, it is vital to understand the relative strength of these interactions, since they lie at the origin of most emergent phases. Usually, it is not enough to focus only on the superconducting phase, as understanding it relies on a broader knowledge of the material's ground state properties, from which not only superconductivity, but also other electronic and magnetic phases emerge. The state of the material is often a fragile balance and tuning parameters like temperature, doping or pressure can be

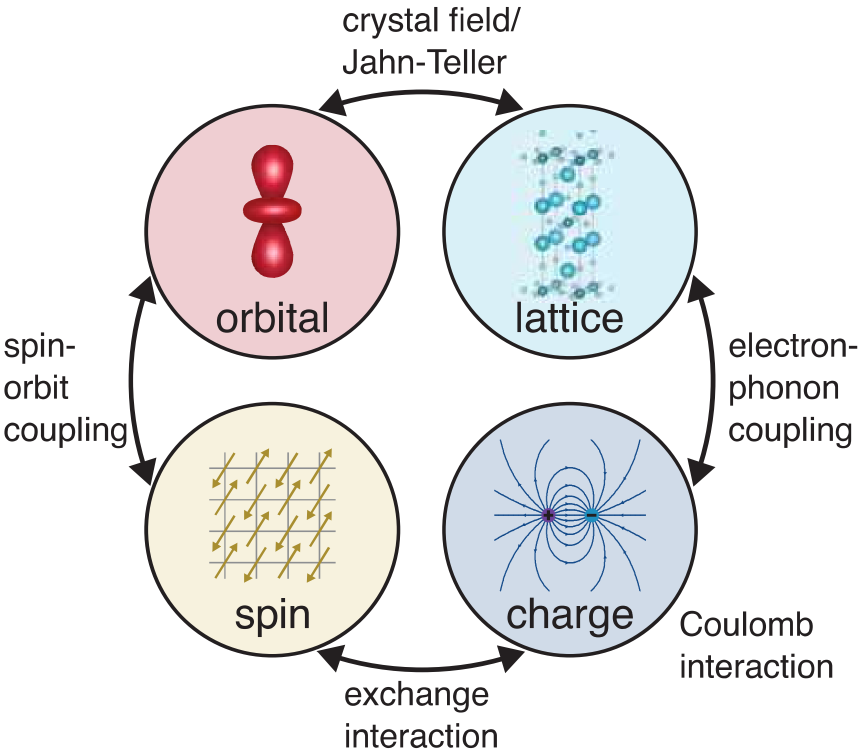

Figure 1.4: Orbital, lattice, spin and charge degrees of freedom. In correlated materials, the different degrees of freedom are coupled with each other by various interactions.

used to induce different phases. Therefore, a holistic approach is necessary to gain an understanding of such correlated materials.

On that background, this thesis focuses on material families where unconventional superconductivity may be present in the phase diagram. However, instead of studying the superconducting phase of these correlated materials directly, the emphasis is placed on surrounding phases and their electronic correlations. The first part in chapter 3 is dedicated to the Mott insulator Ca_2RuO_4, which can be tuned into an unconventional superconductor by Sr substitution, and its sister compound $Ca_3Ru_2O_7$. Resonant inelastic x-ray scattering provides insight into the low-energy excitation spectrum that is defined by energy scales like the crystal field and spin–orbit coupling. The second part in chapter 4 presents a study of the charge order phase in La-based cuprate superconductors, which is known to compete with the superconducting phase. With resonant inelastic x-ray scattering, the charge order can be traced sensitively to determine its temperature and doping extent as well as to probe the electron–phonon coupling. Lastly, the third part in chapter 5 is focused on the superconductor $LiTi_2O_4$. Recent studies suggest an unconventional mechanism behind its superconductivity, drawing parallels to cuprates. The angle-resolved photoelectron spectroscopy study presented here probes the electronic structure in the normal state, giving insight into the electron–phonon coupling strength. Together, these studies are part of a greater endeavour towards the understanding of electronic correlations that define a complex ground state from which phases like unconventional superconductivity emerge.

2 Experimental Methods

This chapter introduces the two main experimental methods used in this study to probe the electronic structures of quantum materials: resonant inelastic x-ray scattering (RIXS) and angle-resolved photoelectron spectroscopy (ARPES). Both techniques are spectroscopic methods that measure the interaction of photons with matter as a function of the photon energy. They are primarily sensitive to the electronic degree of freedom and the energy scales that are responsible for the emergence of exotic phenomena observed in quantum materials. This makes them ideal for the study of correlated systems, which, in turn, has led to substantial improvements in these techniques over the years. In this chapter, both RIXS and ARPES are briefly introduced and explained in a condensed fashion, highlighting only the aspects relevant to this study. Both techniques have numerous other scopes of applications, which have been explored in general reviews [13, 14] and the references therein.

2.1 Resonant Inelastic X-ray Scattering

To understand the relevant degrees of freedom in a material responsible for its macroscopic physical properties, it is essential to gain insight into the relative strengths of the energy scales associated whith lattice, orbital, electronic and magnetic interactions. These include, among other energy scales, crystal field splitting, spin–orbit coupling, magnetic interaction, and electron–phonon coupling. Knowledge of these quantities has proven to be key in understanding emergent phenomena like superconductivity and metal-to-insulator transitions [15, 16], even though their determination is often not straightforward, as the different energy scales can be hard to disentangle. Over the years, various techniques have been established to investigate the strong interplay among different degrees of freedom. For example, neutron scattering is routinely used to measure magnetic properties and low-energy magnetic excitations, whereas the lattice structure is often probed by hard x-ray diffraction. One technique that has been found to be suitable for measuring several degrees of freedom simultaneously is resonant inelastic x-ray scattering (RIXS).

As an advanced inelastic scattering technique, RIXS probes electronic excitations in the material under study. These excitations are usually fingerprints of the underlying low energy scales, and they couple to different degrees of freedom. An example is the spin degree of freedom in a material, which can be probed by RIXS through magnetic excitations called magnons. Therefore, RIXS can provide deep insights into the microscopic phenomena of the material. In the following, the idea behind the technique and the detailed physical process are explained before the technical requirements and data analysis are introduced.

2.1.1 RIXS Scattering Process

Resonant inelastic x-ray scattering is a two-step *photon-in photon-out* technique, in which an incident photon beam impinges on the material under study and the scattered photons are detected as a function of energy and scattering angle. The term *inelastic* refers to the fact that the energy of the scattered photons is resolved, which allows the energy loss of the photons to be determined. This energy loss was transferred to the material in the scattering process, leaving behind excitations in the system. In this way, a broad class of charge-neutral intrinsic elementary excitations can be probed, since the scattered photons neither add charge to nor remove charge from the system. In general, in non-resonant inelastic scattering, the cross section of most electronic excitations is weak, which makes it difficult to retrieve precise information [13, 17]. Therefore, the RIXS technique takes advantage of absorption resonances within the material under study. By tuning the incident photon energy to an absorption edge within the material, the interaction cross section is enhanced, resulting in a two-step process: initially, the photon is absorbed by the system, promoting a core electron to an empty valence state, creating an intermediate excited state, and in the second step, subsequent relaxation occurs by emission of a photon. This process is illustrated in Fig. 2.1.

The first step in this process, the tuning of the incident photon energy to an absorption edge, is the x-ray absorption spectroscopy (XAS) technique. XAS is always performed at the beginning of a RIXS experiment to determine the absorption edge. By itself, it can reveal important information on the electronic structure, as will be shown in chapter 3. An x-ray beam impinges on the material under study and the absorption is measured while varying the incident photon energy E. When E is equal to the binding energy of a core electron, the photon–electron interaction cross section is greatly enhanced and the absorption shows a sharp increase, due to the annihilation of the photon by the creation of a photoelectron and a core hole. The generated excited state, with an electron in the initially unoccupied electronic valence state,

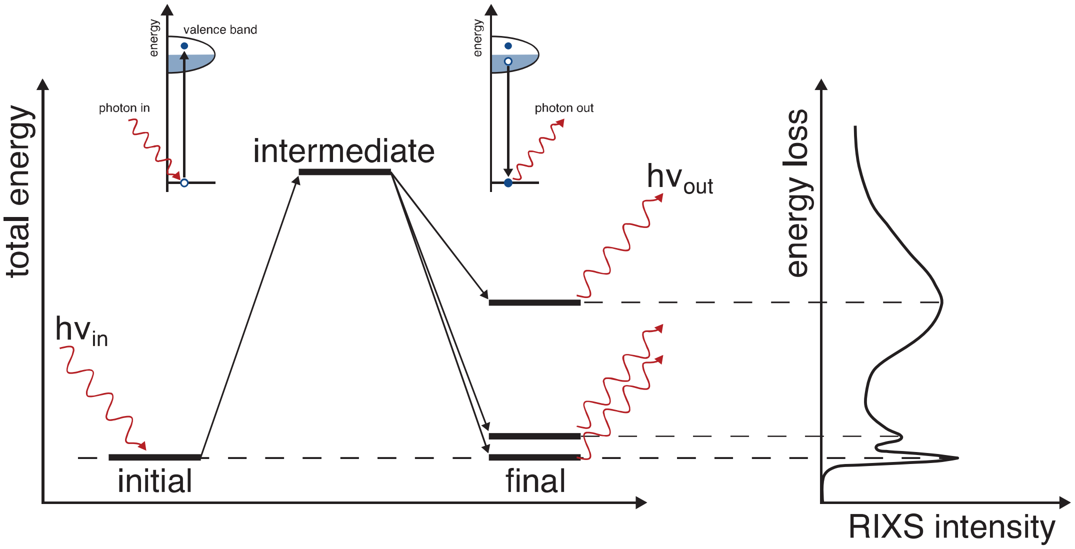

Figure 2.1: Schematic illustration of the RIXS process. After the initial excitation of a core hole, the decay from the excited intermediate state can occur in multiple different ways, leaving behind excitations in the system marked by energy loss features in the RIXS spectrum.

decays on a femtosecond timescale. The core hole is filled by an electron from the valence band, releasing the excess energy via x-ray or Auger electron emission [18].

Naturally, there are absorption edges at all core levels of the different elements and they are classified according to the state of the core electron that is excited. Absorption edges from core electrons with principal quantum numbers $n = 1$, 2 or 3 are called K-, L-, and M-edges, respectively. Since the transition needs to go to an empty valence state of the observed element, the edge energies correspond to the atomic transitions of each element and they increase roughly proportional to Z^2, where Z is the atomic number. This is illustrated in Fig. 2.2a. Thus, each element has specific absorption edges, which can be tuned to in an experiment, making the technique element-specific. This means that by choosing the photon energy in a RIXS experiment at a certain absorption edge, one can choose which element inside the material is investigated. The exact absorption energies are also sensitive to the chemical environment of the atom, for example, sites with inequivalent chemical bondings, atoms with different valencies or at inequivalent crystallographic sites in the crystal structure can lead to a shift in the absorption energy. By examining these shifts, the technique is also sensitive to the crystal field environment. As an example, this becomes important for the oxygen in a layered perovskite structure, which can occupy a planar or apical site, leading to distinguishable features in the absorption spectrum. This is further discussed in chapter 3.

Figure 2.2b shows a general example of copper L_3-edge absorption spectra measured

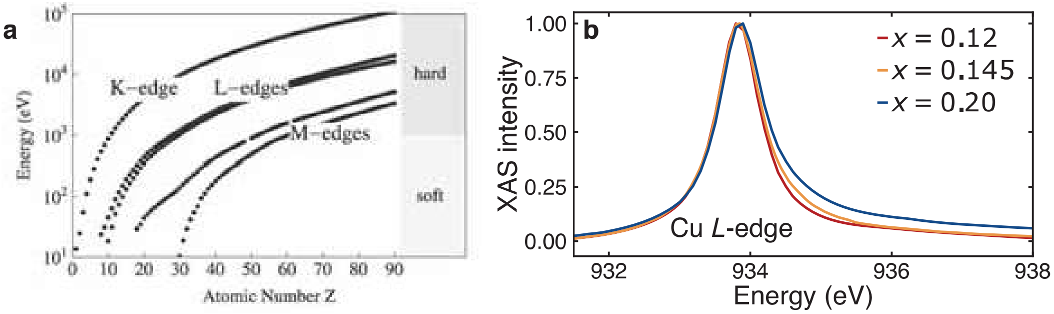

Figure 2.2: X-ray absorption spectroscopy a X-ray absorption edge energy as a function of atomic number Z. From Ref. [13]. **b** Cu L-edge absorption spectra of $La_{2-x}Sr_xCuO_4$ with different dopings x. Recorded at the ADRESS beamline of the Swiss Light Source, 2019.

on $La_{2-x}Sr_xCuO_4$ for different dopings x. At photon energies below 932 eV, there is not enough energy to excite an electron in the copper $2p$ level into the unoccupied states, and therefore no absorption is measured. Above 932 eV, the energy difference between the levels can be overcome by the photon energy and the electrons get excited, resulting in an increase in the absorption of photons. The dipole selection rule for the transition relates the well-defined symmetry of the core electron to the symmetry of the final state: the final state's orbital momentum l increases or decreases by a quantum $\Delta l = \pm 1$ [19, 20]. For the Cu L-edge, this means that the transition goes into a final state with d character. The data is from the Cu L_3-edge, which specifies $2p_{3/2} \rightarrow 3d$ transitions, whereas the L_2-edge has $2p_{1/2} \rightarrow 3d$ transitions. At the O K-edge, the transition is respectively $1s \rightarrow 2p$. Due to this selectivity, it is possible to study not only the energy levels, but also the orbital character of the unoccupied states.

After the first step of the absorption, the electron is in a highly unstable excited intermediate state with a hole deep in the electronic core states. The subsequent decay can occur in multiple different ways, resulting in different final states. In the decay channel relevant for RIXS, the core hole is filled by an electron, with simultaneous emission of a photon. As illustrated in Fig. 2.1, the energy $h\nu_{\text{out}}$ of the emitted photon may or may not be equal as that of the initially absorbed photon, depending on the relaxation process. If the same electron that was previously promoted to the valence shell decays back into the core level before losing energy due to interactions, the emitted photon energy is equal to the incident energy and the process is called elastic scattering. However, if, for example, an electron from an initially occupied valence state recombines with the core hole, the emitted photon has a lower energy and the process is inelastic. The system is now left with an electron–hole excitation that can propagate through the material with energy $h\nu = h\nu_{\text{in}} - h\nu_{\text{out}}$ and momentum $\hbar\boldsymbol{k} = \hbar(\boldsymbol{k}_{\text{in}} - \boldsymbol{k}_{\text{out}})$ [13]. Thus, by measuring the energy of the emitted photon and

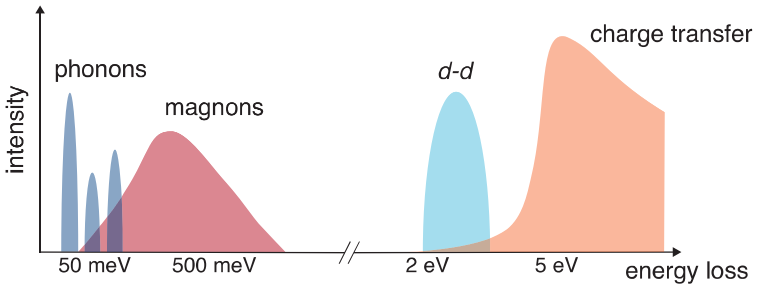

Figure 2.3: RIXS excitations. Schematic illustration of elementary excitations that can be measured by RIXS. The energy scales shown refer to strongly correlated electron materials as investigated in this work. Adapted from Ref. [13].

its angle with respect to the incident photon beam, it is possible to calculate the transferred energy and momentum and with this the momentum dependence of the excitation energy, i.e. its dispersion. In principle, RIXS can also characterize the symmetry and nature of the excitations by analysing the polarization of the incident and scattered photons and using selection rules. A change in polarization of the photon indicates a change in angular momentum. The conservation of angular momentum therefore implies that this change in momentum was transferred to the excitation in the solid.

The RIXS process described above allows for the measurement of a broad range of elementary excitations, including plasmons, charge-transfer excitations, crystal-field and orbital excitations, such as *dd* excitations in transition metal oxides, magnons and phonons [13]. These excitations and their approximate energy scales are shown in Fig. 2.3. The most intuitive are probably the *dd* excitations in transition metal oxides, with partially filled d orbitals that are split by the crystal field. At the metal L-edge, an electron is promoted into an initially unoccupied d state. The subsequent decay can result in an excited configuration if an electron from a different d orbital recombines with the core hole. This can leave, for example, a hole in the lower-lying t_{2g} states and an electron in an initially unoccupied e_g state. Such $t_{2g} \rightarrow e_g$ transitions are the traditional *dd* excitations in the presence of a large crystal-field splitting. If the crystal field is small and the orbital interactions are dominated by superexchange, the orbital excitations have a different character and can move through the crystal, as so-called orbitons [13]. To access magnetic excitations such as magnons in photon scattering processes, the transferred angular momentum of the photon has to be coupled to the valence electron's spin. Although the spin–orbit coupling is usually weak for valence electrons, the intermediate core hole's strong spin–orbit coupling can couple the orbital angular momentum transferred by the photon to the valence electron's spin moment. Detailed discussions of spin excitations can be found in Ref. [13, 21, 22]. For phonon excitations, the detection in a RIXS spectrum depends on the coupling of the excited electronic state to the lattice vibration modes, which is given by the electron–phonon coupling. In the RIXS process, the intermediate state with an extra electron in the valence states and a partially screened core hole can be seen as an altered charge density. Due to this change in charge density, the lattice adapts and deforms. When the intermediate state decays to the original configuration, excited phonon modes are left behind. This will be further discussed in section 4.4. Altogether, RIXS offers a unique way to probe orbital, charge, magnetic and lattice degrees of freedom via their excitations in a single spectrum. As discussed, the use of resonances allows furthermore the targeting of specific elements or orbitals in the material.

This work focuses on soft x-ray RIXS (200-3000 eV), in which the penetration depth is on the order of 100 nm. This is classified as a bulk-sensitive probe, compared to surface-sensitive techniques like angle-resolved photoelectron spectroscopy. Another advantage of RIXS is the ability to perform experiments on small sample volumes compared to neutron scattering. This allows for experiments on thin films, atomic layers or nano-objects. Since RIXS relies on photon scattering, it can in principle also be performed in electric or magnetic fields, as well as under high pressure. All these advantages of RIXS make it a powerful technique that can be applied to a wide range of materials. However, like all experimental techniques, RIXS has limitations, lying mainly in its energy-resolving power. This is determined by the availability of tunable photon sources providing a high enough photon flux, and the ability of the instrumentation to energy resolve the scattered photons. Although the energy resolution has improved significantly in the last decades, it cannot yet compete with other techniques, such as inelastic neutron scattering for the study of e.g. low-energy phonons or magnons. In addition to the limitated resolving power, the strictly reflective scattering geometry of RIXS limits the reciprocal space that can be measured to the first Brillouin zone. In fact, for compounds like the ruthenates or cuprates discussed in the following chapters, the in-plane momentum space is limited to half of the first Brillouin zone or less. Different techniques are usually complementary, covering different energy and momentum regions, elementary interactions or sample sizes. In recent decades, RIXS instrumentation has advanced significantly, offering substantially higher energy resolution. After a brief discussion of the theoretical aspects, section 2.1.2 will introduce the technical requirements that enabled this improvement in resolution.

Kramers–Heisenberg Equations

To describe the theory behind the RIXS process, the two-step scattering process, from the initial state, over a short-lived intermediate state, to the final state, needs to be considered. This picture includes the electron system in the solid, the electromagnetic field of the photon, and the interactions between them. Here, the RIXS cross section in the form of the Kramers–Heisenberg equations is briefly outlined; a full derivation can be found in Ref. [13].

To compute the RIXS intensity, the scattering amplitude describing the interaction of photons and matter needs to take into account energy conservation and the probed excitations depending on the photon polarization. The starting point is usually the Hamiltonian describing the electron system in the solid, the incident x-ray beam, and the interaction between them. Since the interactions are usually small, they can be treated perturbatively. Therefore, the Hamiltonian is divided into H_0, describing the system under study, and the electron–phonon interaction term H', which can then be treated as a perturbation of H_0.

Fermi's golden rule up to second order gives the transition rate for a single photon in initial state $(\boldsymbol{k}, \omega_{\boldsymbol{k}}, \boldsymbol{\epsilon})$ – where $\hbar\boldsymbol{k}$ is the momentum, $\hbar\omega_{\boldsymbol{k}}$ is the energy and $\boldsymbol{\epsilon}$ the polarization – that is scattered to the final state $(\boldsymbol{k'}, \omega_{\boldsymbol{k'}}, \boldsymbol{\epsilon'})$ while inducing a change in the material from ground state $|g\rangle$, over intermediate state $|n\rangle$ to final state $|f\rangle$ with energies E_g, E_n and E_f, respectively:

$$\begin{aligned} w = & \frac{2\pi}{\hbar} \sum_{f,\mathbf{k}',\boldsymbol{\epsilon}'} \left| \langle f; \mathbf{k}'\boldsymbol{\epsilon}' | H' | g; \mathbf{k}\boldsymbol{\epsilon} \rangle + \sum_n \frac{\langle f; \mathbf{k}'\boldsymbol{\epsilon}' | H' | n \rangle \; \langle n | H' | g; \mathbf{k}\boldsymbol{\epsilon} \rangle}{E_g + \hbar\omega_{\mathbf{k}} - E_n} \right|^2 \\ & \cdot \delta(E_f + \hbar\omega_{\mathbf{k}'} - E_g - \hbar\omega_{\mathbf{k}}) \, . \end{aligned} \tag{2.1}$$

The initial, intermediate and final states are all eigenstates of H_0. The first term describes the first-order amplitude coming from non-resonant scattering processes with a direct transition from the initial to the final state and usually dominates. However, if the incident x-rays are tuned to a transition in the material, i.e. if $E_g + \hbar\omega_{\boldsymbol{k}} \approx E_n$, then the second term describing the second-order amplitude dominates. This term causes the resonant scattering relevant in RIXS and, therefore, the first-order term is neglected from now on.

The only terms of H' relevant for resonant scattering are those linear in the electromagnetic vector potential $\boldsymbol{A}(\boldsymbol{r}, t)$. Furthermore, the magnetic term is small compared to the nonmagnetic term and so can also be neglected. The resulting transition operator for the resonant RIXS cross section then becomes

$$\mathcal{D} = \frac{1}{im\omega_{\mathbf{k}}} \sum_{i=1}^{N} e^{i\mathbf{k}\mathbf{r}_i} \boldsymbol{\epsilon} \cdot \mathbf{p}_i \, . \tag{2.2}$$

Equations (2.1) and (2.2) can now be used to compute the double-differential cross section $I(\omega, \boldsymbol{k}, \boldsymbol{k'}, \boldsymbol{\epsilon}, \boldsymbol{\epsilon'})$:

$$I(\omega, \mathbf{k}, \mathbf{k}', \boldsymbol{\epsilon}, \boldsymbol{\epsilon}') = r_e^2 m^2 \omega_{\mathbf{k}'}^3 \omega_{\mathbf{k}} \sum_f \left| \mathcal{F}_{fg}(\mathbf{k}, \mathbf{k}', \boldsymbol{\epsilon}, \boldsymbol{\epsilon}', \omega_{\mathbf{k}}, \omega_{\mathbf{k}'}) \right|^2 \delta(E_g - E_f + \hbar\omega) \tag{2.3}$$

$$\mathcal{F}_{fg}(\mathbf{k}, \mathbf{k}', \boldsymbol{\epsilon}, \boldsymbol{\epsilon}', \omega_{\mathbf{k}}, \omega_{\mathbf{k}'}) = \sum_n \frac{\langle f|\mathcal{D}'^{\dagger}|n\rangle \ \langle n|\mathcal{D}|g\rangle}{E_g + \hbar\omega_{\mathbf{k}} - E_n + i\Gamma_n} \,, \tag{2.4}$$

where $r_e = (1/4\pi\epsilon_0)e^2/mc^2$ is the classical electron radius. These are known as the Kramers–Heisenberg equations describing the RIXS process. In the scattering amplitude $\mathcal{F}_{fg}$, a life-time broadening Γ_n is introduced for intermediate states n, accounting for the nonradiative interaction terms like Auger decay that are not included in H' and which make the intermediate states short-lived.

To simplify and proceed from these equations, one can first separate the parts related to the geometry of the experiment, which come from the photon momentum and polarization vectors, from the parts related to the fundamental scattering amplitude, which come from the physical properties of the material under study. To evaluate the fundamental scattering amplitude, a Hamiltonian for the system under study is constructed, which focuses on the relevant terms for the probed excitations. From this, a numerical or approximative approach can be used to determine the RIXS amplitude. For example, the scattering amplitude can be evaluated numerically on a small cluster of atoms; see chapter 3. In the approach used in that chapter, the focus is on spin–orbital excitations and the Hamiltonian is composed of electron–electron, spin–orbit and crystal-field terms. The eigenstates and eigenvalues for the ground, intermediate and final states are evaluated by exact diagonalization of this Hamiltonian for the defined cluster. These are then used to evaluate the scattering amplitude. Even though this approach is effective at capturing the electronic correlations, the basis set grows rapidly, so that usually only a cluster of a few atoms is considered. This in turn does not allow effective modelling of collective phenomena and delocalization. For the theory behind the phonon study presented in section 4.4 [23, 24], the adopted Hamiltonian, consisting of the electron–phonon coupling term and the phonon term, is diagonalized by a canonical transformation to evaluate the scattering amplitude. Alternative approaches neglect electronic correlations or resort to an effective single-particle description [13]. Which approach is most effective depends strongly on the material and the specific RIXS process under investigation.

2.1.2 Technical Requirements

RIXS is an advanced scattering technique, in which several technical aspects need to work together to combine the resonant excitation with an inelastic scattering process. First, a monochromatic, tunable photon beam needs to be focused on the material under study, and then the scattered photons need to be detected and their energies resolved for a specific scattering angle. For modern RIXS experiments on three-dimensional materials, one needs to be able to measure at an arbitrary point in reciprocal space, which requires the ability to rotate the sample about three independent rotation axes in addition to the variable scattering angle. The whole experiment must also be performed under ultra-high vacuum to avoid loss of the photons, and the sample must be cryogenically cooled to access the novel behaviour of quantum materials, which typically occurs below 50 K. Altogether, the experiment is a tremendous technical challenge.

The technical implementations depend on the absorption edges, i.e. the photon energies, that are used. They are categorized into soft and hard x-ray RIXS instruments. In hard x-ray instruments, Bragg crystal optics are used, with the highly ordered crystalline lattices of Si or Ge achieving a very high energy resolution. However, this does not work in the soft x-ray regime, because the longer wavelength does not match the crystal lattice. Instead, artificial periodic structures like diffraction gratings are used. In this work, soft x-ray RIXS was employed and therefore this section focuses on the instrumentation for this specific photon energy region. The RIXS instrument itself can be divided into three parts:

- the beamline, which provides a collimated, focused and highly monochromatic photon beam
- the sample environment, with a manipulator that provides several rotation and translation stages, as well as cryogenic cooling
- the spectrometer where the scattered photons are focused and energy-dispersed before reaching the detector at the end

The three parts are illustrated in Fig. 2.4 for an example RIXS beamline. In the following, the three parts and their respective requirements are introduced for the beamlines utilized in this work: the ADRESS beamline at the Swiss Light Source (SLS, Switzerland), the ID32 beamline at the European Synchrotron Radiation Facility (ESRF, France) and the I21 beamline at the Diamond Light Source (Diamond, UK).

Beamline

To tune the incident photon energy to an absorption edge in the material, and also to have full control over the polarization, the photon source in RIXS beamlines is an undulator insertion device in a synchrotron storage ring, where electron bunches are

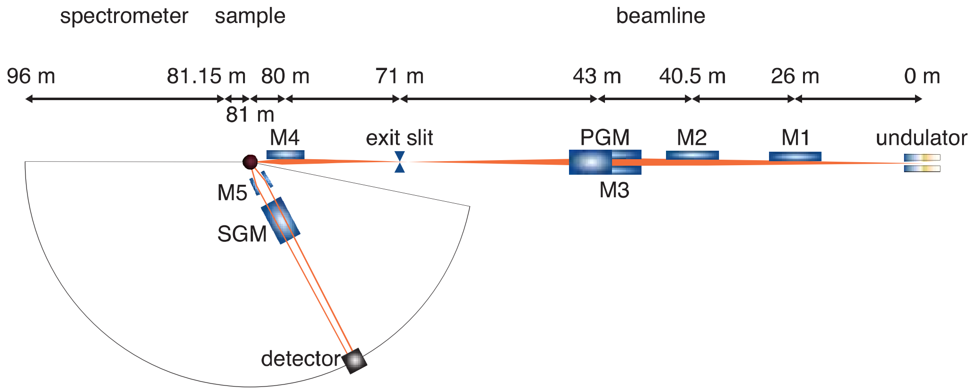

Figure 2.4: RIXS beamline. Layout of the I21 beamline at the Diamond Light Source from above. Adapted from Ref. [25].

kept in a circular accelerator. The undulator consists of periodic dipole magnets, whose magnetic field alternates along the length of the device. Therefore, the electrons passing through the device are forced into oscillations with the wavelength of the magnets, and since accelerated charged particles produce radiation, the device can be used as a radiation source. Because of the relativistic speed of the electrons, the emission profile is highly directional, i.e. focused. The radiation created in this way is also very intense and coherent: ideal for the photon-hungry RIXS technique. After the undulator, the beamline optics, which consist of several mirrors and a monochromator, focuse the photon beam and select a specific energy. At the ADRESS beamline, this is done with a collimated-light plane grating monochromator (PGM) [26], while the ID32 and I21 beamlines use variable line spacing (VLS) PGM [25, 27]. The covered energy ranges at ADRESS and ID32 are similar at 400-1800 eV and 400-1600 eV, respectively. I21 was designed to cover a wide range of energies from 280-3000 eV, including most $4d$ L-edges and some $5d$ M-edges. Altogether, the beamline provides a highly monochromatic polarized beam with a high flux and a small spot size on the sample.

Sample Environment

As mentioned above, the transferred momentum of the scattered photons is related to the momentum of the excitations left behind in the material under study. Therefore, the scattering geometry with respect to the sample lattice needs to be controlled carefully. To do so, the sample is mounted on a manipulator allowing for precise rotational and translational orientation. At ID32, for example, a four-circle ultra-high vacuum (UHV) diffractometer is used [27]. The manipulator also provides cooling to the sample via a helium flow cryostat. Typical sample base temperatures at the above-mentioned RIXS beamlines are around 20 K.

As explained above, the first step in a RIXS experiment is the measurement of the resonance energy by XAS. The absorption spectrum can be detected in different ways, depending on the sample and its environment. The most direct method is transmission mode measurement [28], which is, however, not practical when the sample is mounted on the previously described manipulator setup for reflection RIXS experiments. Transmission also requires homogeneously thin samples, whereas this study focuses on bulk single-crystal samples. Therefore, the more suitable methods for absorption measurements before a RIXS experiment are based on reflection and make use of the relaxation process after the absorption. The core hole is filled by an electron in the valence band on a femtosecond timescale. The energy difference of that electron can be released in two ways: either a photon is emitted (this isalso the relevant process for RIXS, called fluorescence) or the energy is transferred to another electron in the valence band, which is then promoted to an unoccupied state and eventually escapes into vacuum (Auger electrons). The decay products for the two pathways, the emitted photon or electron, can be measured and the respective XAS modes are called fluorescence yield and electron yield mode.

In total electron yield mode, the emitted electrons are measured by grounding the sample on the manipulator and detecting the drain current to the sample when the emitted electrons are replaced. The drain current is proportional to the number of absorbed photons and is therefore an indication for the absorption spectrum. The Fermi level of the system is not affected by the process and charge neutrality is preserved.

In total fluorescence yield mode, a photodiode in the sample chamber is used to measure the intensity of the emitted x-rays from the radiative relaxation of the core hole. The intensity of the fluorescence line integrated over a finite solid angle and a broad range of energies is proportional to the absorption. Furthermore, the fluorescence intensity corresponds to the integrated RIXS intensity at the same angle and incident energy. A drawback of this measurement mode is the self-absorption, which also needs to be taken into account for RIXS measurements. If the outgoing angle of the emitted photon is very low, the travelling path inside the sample is long and the photon may be reabsorbed before it can be detected.

RIXS Spectrometer

After tuning the incident photon energy to the absorption edge by XAS, the last part of the RIXS instrumentation, the spectrometer, analyses the energy of the scattered photons. It consists of several components. At ID32 and I21, a parabolic collecting mirror immediately after the sample guarantees a high photon throughput for the spectrometer. Next, a grating energy-disperses the scattered photons vertically

Figure 2.5: Spectrometer image. RIXS spectrometer at the I21 beamline of the Diamond Light Source. From Ref. [25].

before they hit the detector at the end of the spectrometer. Photons with different energies are scattered off the grating with different angles such that the vertical impact location on the detector corresponds to their energy. Therefore, a longer spectrometer arm increases the spatial distance on the detector for photons with a given energy difference ΔE, and allows for a higher energy resolution. Fig. 2.5 shows the I21 beamline and its spectrometer as an example. However, the spectrometer length is not the only contribution to the energy resolution. To achieve high resolution, the undulator and monochromator in the beamline also play important roles, as well as the tuning of the monochromator to the spectrometer and the contribution from each optical element. Additionally, the detector and its spatial resolution have a significant impact on the total resolution. Depending on the photon energy, the detector height and inclination need to be adjusted accordingly to guarantee optimal detection conditions. In the following, the spectrometers and their specifics are introduced for the three beamlines used in this work.

At ADRESS, a RIXS beamline operational since 2007, the spectrometer has a total length of 5 m from the sample to the detector and is based on a VLS spherical grating, which focuses the photons on the detector in addition to the dispersing the energy of the scattered photons. The spectrometer has two gratings with different line spacings, offering either high-resolution or high-throughput measurements. The detector RIXSCam, from XCAM Ltd., is an electron multiplying charge-coupled device (CCD), consisting of three horizontally arranged chips for reduced acquisition time. The total energy resolution at the Cu L_3-edge ($\approx 930\,\mathrm{eV}$) is $80\,\mathrm{meV}$ [26].

At ID32, a new generation of high-resolution RIXS beamlines, the total spectrometer length is 12 m and two VLS spherical gratings are used. At the end of the spectrometer, before the detector, there is also a polarimeter, which allows analysis of the polarization of the scattered photons. This feature has not been used in this work and is therefore not discussed here: information can be found in Ref. [27]. In the high-resolution operating mode, at the Cu L_3-edge, a combined resolution of 30 meV can be achieved [27]. In addition to the high energy resolution, the entire 12 m long spectrometer arm can be moved continuously over 100° to change the scattering angle between 50° and 150°. This allows for measuring arbitrary points in reciprocal space. To achieve this rotation, the spectrometer's steel structure is mounted on air pads and a pressure of 5 bar can raise the scattering arm by approximately 70 µm, allowing for it to be moved.

At I21, the total spectrometer length is 15 m and three VLS spherical gratings are used to cover the broad range of 280-3000 eV. In the high-resolution operating mode, a combined resolution of 35 meV can be achieved at the Cu L_3-edge [25]. Apart from the broader energy range at this beamline, special focus was put on a high x-ray photon throughput, achieved by using a long undulator source, minimizing the number of optics, optimizing the mirror reflectivities and situating the collecting mirror in front of the spectrometer very close to the sample. Similarly to ID32, the spectrometer arm at I21 is lifted by air pads and can be continuously rotated about the sample position over 150°.

Sample Preparation

For a successful RIXS measurement, not only are the beamline and endstation crucial, but also the sample preparation. To relate the transferred momentum of the photons to the momentum of the excitation within the material, the sample orientation needs to be known. In this work, single crystals were investigated that have been aligned ex situ with a back-reflection Laue x-ray diffractometer before the experiment to orient the crystallographic axes. In short, the Laue technique uses a polychromatic x-ray beam, which is focused on the sample, and the backscattered photons are detected by a two-dimensional detector screen. The Bragg condition is fulfilled by several crystal planes, since the incident photon beam contains many different wavelengths, and multiple diffraction peaks are visible on the detector. One can identify high-symmetry planes and the crystal axes by rotating the sample and tracking the diffraction pattern. As an example in $Ca_3Ru_2O_7$, Fig. 2.6a and b show the measured and simulated diffraction pattern in the ab-plane that is typical for perovskite materials. The different axes along the Ru–O and Ru–Ru bond directions can be identified because of higher-order reflections. The two axes have an angle

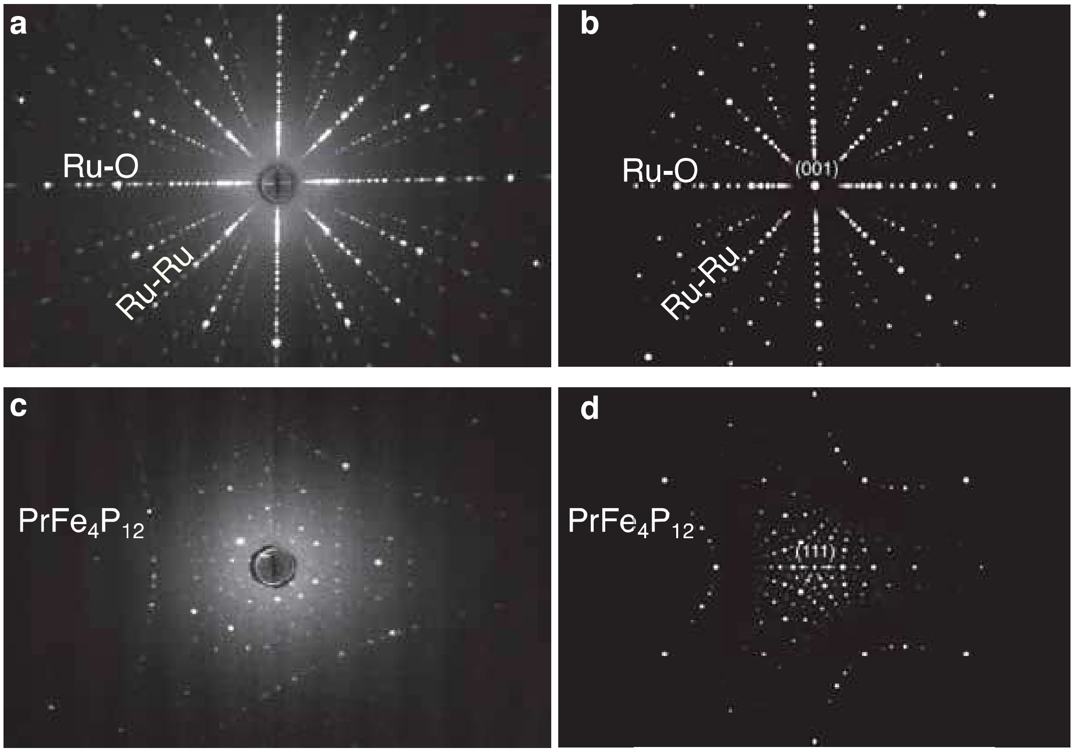

Figure 2.6: Single crystal orientation with Laue. **a** Measured Laue pattern of $Ca_3Ru_2O_7$ in the *ab*-plane. Adapted from Ref. [29]. **b** Simulated Laue pattern corresponding to the measured pattern in **a**. The bond directions in the crystal can be assigned according to the known directions in the simulated pattern. **c** Measured Laue pattern of $PrFe_4P_{12}$ with the (111) crystal axis pointing out-of-plane. **d** Corresponding simulated Laue pattern. **b, d** Courtesy of P. Usai.

of 45° between them but the higher-order reflections are closer to the Ru–Ru bond direction. This is also seen in the simulated Laue pattern on the right. As another example, in Fig. 2.6c and d, measured and simulated Laue patterns are shown for $PrFe_4P_{12}$ with space group $Im\bar{3}$ oriented along the (111) crystal axis. Before the experiment, the principal crystal axes are marked close to the sample to allow RIXS measurements along a specified direction.

Apart from the crystal orientation, the crystal surface also needs to be considered in a RIXS experiment. For good data quality, a low surface roughness is important, since soft x-rays have a shorter penetration depth, and diffuse scattering on the surface leads to fewer photons on the detector, so should be minimized in a photon-hungry technique like RIXS. In order to obtain a flat and clean crystal surface, the sample is cleaved – i.e. cut or broken up along an atomic crystal plane, in situ under high vacuum. For this, a top-post is glued on the sample prior to the experiment, which can be hit by a wobble stick in the vacuum chamber to break off the top part of the

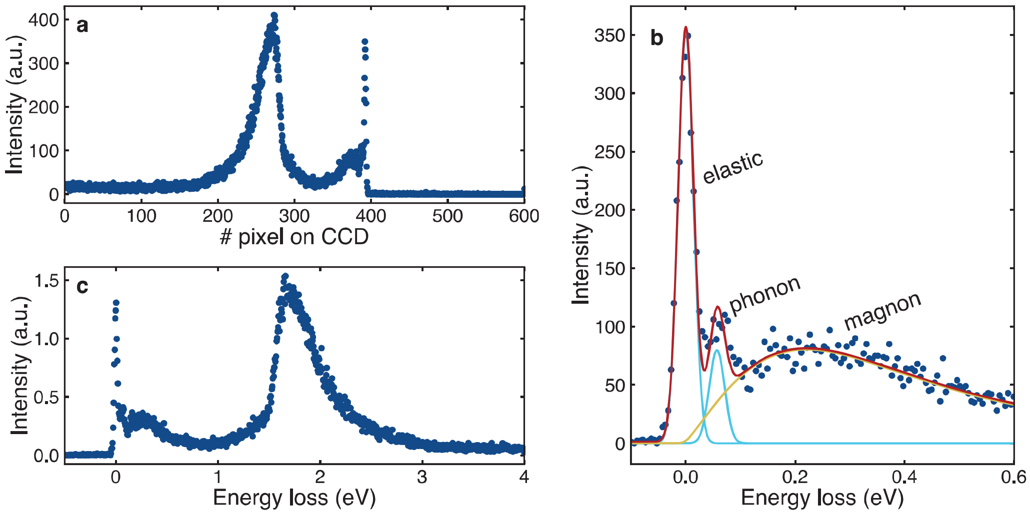

Figure 2.7: Energy scale calibration. **a** Raw spectrum from the CCD detector, horizontally integrated. **b** Fitting of the low-energy part of the spectrum to determine zero energy loss from the peak position of the elastic peak. Dark blue dots are the recorded intensity, whereas the red line represents the total fit with two Gaussian components for the elastic and phonon line and a damped harmonic oscillator response function for the magnon contribution. **c** Final spectrum with adjusted energy scale and intensity normalized to the integrated weight of the *dd* excitations.

sample, leaving behind a fresh and clean surface.

2.1.3 Data Analysis

Once a RIXS experiment has been successfully conducted, the data are analysed to extract comprehensive information about the excitations in the spectrum. This section briefly summarizes the most important steps of calibrating the energy scale and normalizing the intensity, allowing quantitative comparison of different spectra and then calculating the momentum transfer for a certain experimental geometry.

Energy Scale Calibration

As described above, the scattered photons are dispersed in the spectrometer and their vertical impact height on the detector depends on their energy. One can thus relate the vertical impact position on the CCD to the energy loss of the photon. The detector is two-dimensional, allowing integration along the horizontal direction for improved statistics. Since the spectrum can have a certain inclination on the CCD depending on the exact positions of the grating and the detector, most beamlines provide a slope-corrected integration of the measured two-dimensional signal to provide a one-dimensional spectrum of intensity as a function of vertical CCD pixel number. The counting time for each spectrum depends on the intensity of the scattered beam and the statistics required. To avoid overexposure of the CCD, the spectrum is read out after a certain time and the measurement is repeated under the same conditions until the desired statistics are obtained. In this way, several spectra are produced belonging to a single measurement, and need to be combined. Since the exact position of a photon with a certain energy on the detector can shift over time, the different spectra cannot immediately be added, but must first be correlated to account for the pixelshift. After the correct horizontal integration and correlation, a single spectrum for one measurement is obtained. As an example, Fig. 2.7a shows the spectrum of $La_{2-x}Sr_xCuO_4$ with $x = 0.145$ obtained in this manner.

In the next step, the pixel axis of the spectrum is converted to an energy loss scale. In the recorded spectrum, each pixel channel corresponds to a specific photon energy, and the energy difference between two channels is specific for an incident photon energy and spectrometer settings. Therefore, the energy per pixel needs to be determined after every change of the absorption edge by calibration on a carbon tape. An amorphous carbon tape is used as a reference, which only shows an intense, resolution-limited elastic peak on the detector. As the incident photon energy is varied, the peak moves vertically over the detector and the energy per pixel can be determined. Additionally, this method allows for the determination of the total energy resolution of the specific measurement as the full width at half maximum (FWHM) of the measured elastic peak. Knowing the energy per pixel, one can convert the pixel axis of the spectrum to an energy axis. However, the absolute energy of one pixel is not known *a priori* and depends on the detector height. Over long measurements, this absolute energy position can also drift on the detector. Therefore, one needs to measure the carbon tape regularly during the measurement or evaluate the absolute energy of a pixel for each spectrum in the data analysis process by determining the elastic peak. From experience, the latter has proven to be more reliable and was applied in this work.

The probability of a photon gaining energy in the scattering process is usually negligible, which means that the incident photon energy is the upper limit for the detected energies. Thus, the first signal on the high-energy side comes from elastic scattering, with $h\nu_{\mathrm{in}} = h\nu_{\mathrm{out}}$. In Fig. 2.7a, the high-energy side corresponds to higher pixel numbers, so the first peak around pixel 400 is the elastic peak and marks zero energy loss of the photons. For an exact determination of the zero energy loss as the centre of the elastic peak, the low-energy part is fitted. The fitting procedure is especially important in cases where the elastic peak overlaps with low-energy excitations. In the example shown, there are phonon and magnon peaks close to the elastic peak, which have therefore been included in the fitting procedure; see Fig. 2.7b. The elastic and phonon peaks are modelled with a Gaussian lineshape, with the width of the elastic Gaussian fixed to the resolution, whereas, for the magnon, a response function of a damped harmonic oscillator (DHO) [30] is used. Since the fit is sensitive to the fitting range, a fixed window is chosen and, as a start, the elastic line is set roughly to zero. After the fit, the energy scale is shifted by the offset of the centre of the elastic peak to energy zero and the fitting and adjusting of the energy scale is repeated until the shift falls below an acceptance limit. Another approach is to only take the data points from the left of the elastic peak in Fig. 2.7b up to shortly after the peak maximum and fit this region to determine the centre of this peak. Which method is used depends on the intensity of the elastic peak and how significant the overlap with low-energy excitations is.

Once the energy scale has been determined, the intensity of the whole spectrum needs to be normalized to allow comparison of spectra recorded with different geometries. There are different methods of normalization and the most suitable one has to be chosen case by case. For example, one can normalize the spectrum to the integral of a certain energy range in the spectrum that shows no excitation signal. Another method, which was applied in this study, is to normalize to the integrated weight of the *dd* excitations of the studied sample. In the example in Fig. 2.7c, the integration range was 1-4 eV. This method has proven reliable, since the total spectral weight of the *dd* excitations does not vary significantly for different measurement conditions. It is also favourable over a normalization to a featureless area of the spectrum, since most correlated materials have very rich low-energy excitation spectra, and it is not always possible to find a range without a contribution from an excitation.

Momentum Transfer Calculation

This section briefly explains how the momentum of the excitation can be inferred from the experimental geometry. Due to momentum conservation in the scattering process, the momentum transferred to the excitation is equal to the change in momentum of the scattered photon, which can be inferred from the experimental geometry. In Fig. 2.8a, the incident and outgoing paths of the photon are depicted with respect to the sample orientation. In an experiment, the scattering angle γ between the incident and outgoing beams is set by the respective position of the beamline and the spectrometer arm. Furthermore, the change in the absolute value of the photon momentum is negligible, since an energy difference of a few electronvolts only changes the photon momentum by several $10^{-3}\,\text{Å}^{-1}$, from a total momentum for soft x-rays on the order of $10^{-1}\,\text{Å}^{-1}$. The elastic case of $k_{\text{in}} \approx k_{\text{out}}$ is therefore assumed for the calculation. From the total momentum transferred $\boldsymbol{q}_{\text{tot}}$, the relevant part when

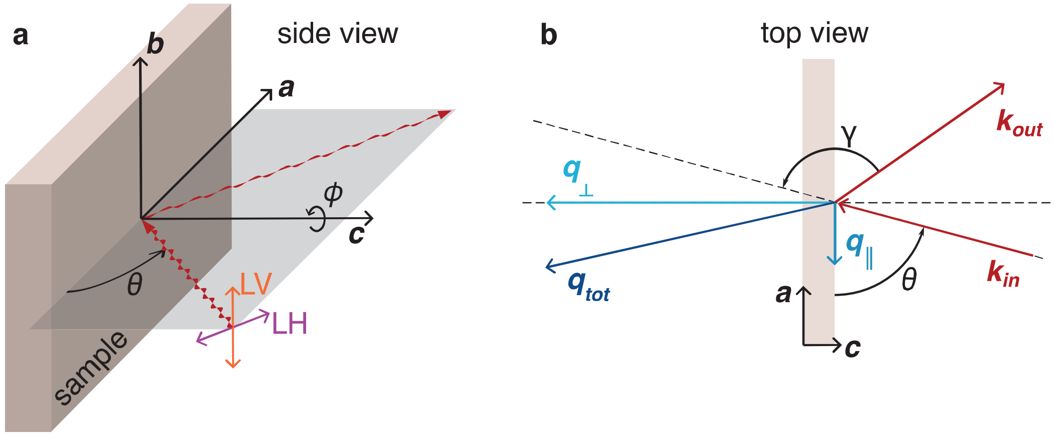

Figure 2.8: Experimental geometry and transferred momentum. **a** The incoming photons $\boldsymbol{k}_{\text{in}}$ (red arrows) have an incident angle θ with respect to the sample surface and their polarization is linear vertical (LV, perpendicular to the scattering plane) or linear horizontal (LH, in the scattering plane). **b** The momentum change $\boldsymbol{q}_{\text{tot}} = \boldsymbol{k}_{\text{out}} - \boldsymbol{k}_{\text{in}}$ is split into the components parallel and perpendicular to the sample surface ($-\boldsymbol{q}_{\text{tot}}$ is plotted for clarity).

measuring layered systems is usually the projection onto the sample ab-plane. The total momentum is therefore split into the contributions parallel and perpendicular to the ab-plane. For the experiment, the sample is oriented such that its c-axis lies within the scattering plane and the sample surface corresponds to the ab-plane. By rotating the sample around θ, the angle between the incident photon beam and the sample surface is changed, and with this the in-plane momentum transfer is varied. Furthermore, the reciprocal space is expressed in terms of Miller indices by $\boldsymbol{q} = h\boldsymbol{a}^* + k\boldsymbol{b}^* + l\boldsymbol{c}^*$ where $\boldsymbol{a}^*$, $\boldsymbol{b}^*$ and $\boldsymbol{c}^*$ are the reciprocal lattice vectors. Altogether, the in-plane momentum component h becomes (Fig. 2.8b):

$$\begin{aligned} |\boldsymbol{q}_{\text{tot}}| &= |\boldsymbol{k}_{\text{out}} - \boldsymbol{k}_{\text{in}}| = 2k_{\text{in}} \sin(\gamma/2) \\ q_{\parallel} &= |\boldsymbol{q}_{\text{tot}}| \sin(\theta - \gamma/2) \\ q_{\perp} &= |\boldsymbol{q}_{\text{tot}}| \cos(\theta - \gamma/2) \\ h &= \frac{q_{\parallel}}{2\pi/a}. \end{aligned} \tag{2.5}$$

The orientation of $q_{\parallel}$ within the lattice plane can be varied by rotating the sample around the c-axis by the angle ϕ. In the layered perovskite lattice structures, to which $\mathrm{Ca}_{n+1}\mathrm{Ru}_n\mathrm{O}_{3n+1}$ and $\mathrm{La}_{2-x}\mathrm{Sr}_x\mathrm{CuO}_4$ belong, the direction of interest is usually the a/b-axis or the diagonal.

2.2 Angle-Resolved Photoemission Spectroscopy

The physical properties of a material that are relevant for technological applications typically include its resistivity, specific heat and magnetization, among others. These macroscopic observables can often be measured straightforwardly, but for a profound understanding of their origin and behaviour under changing conditions, the microscopic mechanisms in the material need to be investigated with all methods available. As described in the previous section, RIXS tackles the problem by inferring information about the different energy scales associated with lattice, orbital, electronic and magnetic interactions. Another approach is to directly look at the electronic band structure of the material. Since many of the most intriguing phenomena emerge from electronic interactions, the so-called electronic correlations, the knowledge of the electronic structure is in most cases vital for the understanding. The most direct measurement method is angle-resolved photoemission spectroscopy (ARPES), which probes the electronic dispersion, i.e. the relation between the electron's energy and momentum through the spectral function. ARPES can also give insight into electron–phonon interaction, electron–electron interaction and spin–orbit coupling through their signatures in the spectra.

ARPES is a *photon-in electron-out* experimental technique that is based on the photoelectric effect [31], which is the emission of electrons upon irradiation of a material with electromagnetic radiation. The effect was explained by Albert Einstein in 1905 [32] using the concept of light quanta, a concept earlier introduced by Max Planck [33]. This laid the foundation for the introduction of quantum physics and shaped our understanding of the world we live in. But the photoelectric effect also offered a direct way to investigate the electronic structure of a material via the photoemission process, since the emitted electron's energy and momentum distribution can be traced back to its dispersion, under certain assumptions. In the following, the photoemission process and the working principle of ARPES are briefly explained with a focus on the aspects relevant to this study. The discussion presented here follows closely the relevant parts of the reviews of Damascelli and Sobota [14, 34]. More detailed and broader views on ARPES can be found in these reviews and other literature [14, 34, 35, 36, 37]. After outlining the method, its technical requirements and the data analysis procedures adopted in this work are presented.

2.2.1 ARPES Photoemission Process

In the photoemission process, the material under study, the so-called sample, is irradiated by a light source. The photons excite electrons, which are then released

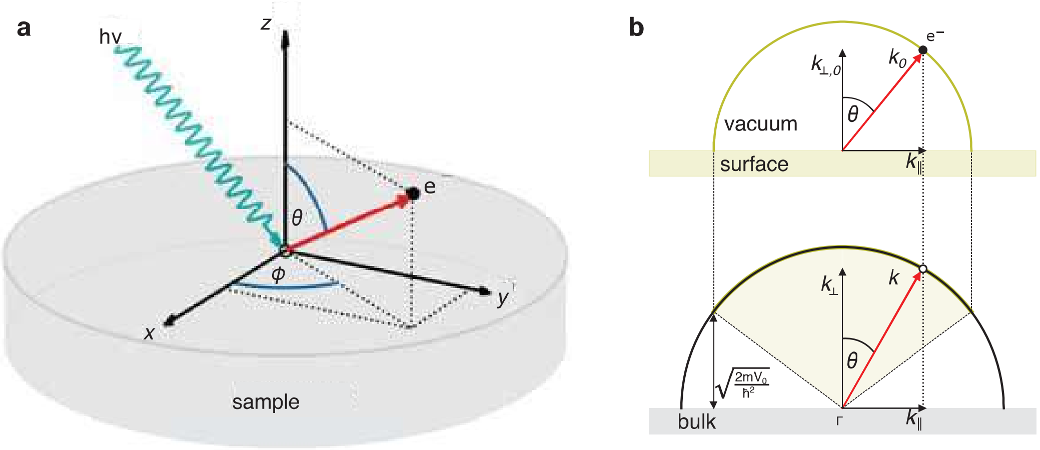

Figure 2.9: ARPES schematic. **a** Illustration of the *photon-in electron-out* geometry including the polar angle θ and azimuth angle ϕ. **b** Conservation of momentum parallel to the surface upon transmission through the surface. Adapted from Ref. [37].

from the material. In an ARPES measurement, a fraction of these emitted electrons are detected by a photoelectron spectrometer to infer their kinetic energy E_{kin} and emission angles (θ, ϕ) from the sample surface. As depicted in Fig. 2.9a, θ is the polar angle with respect to the surface normal z, and ϕ is the azimuth angle with respect to the in-plane crystal axis x. In an ARPES measurement, the light source provides monochromatic radiation of energy $h\nu$, and the binding energy E_B prior to the emission relative to the sample's Fermi level E_F, as well as the crystal momentum $\hbar\boldsymbol{k}$ of the electrons, can be deduced by employing energy and momentum conservation laws:

$$E_{\text{kin}} = h\nu - \Phi - E_B \tag{2.6}$$

$$\hbar\boldsymbol{k}_{\parallel} = \sqrt{2mE_{\text{kin}}}\,\sin(\theta) \tag{2.7}$$

where Φ is the material's work function[1], m is the electron's mass and $\hbar\boldsymbol{k}_{\parallel}$ is the component of the crystal momentum parallel to the surface. In Eq. (2.7), the photon momentum is omitted since it is negligible for the ultraviolet range used in this study. Note that it must be considered in the soft and hard x-ray ranges. The momentum $\boldsymbol{k}_{\parallel}$ is conserved in the photoemission process due to the discrete in-plane periodicity of the crystal structure; see Fig. 2.9b. The perpendicular component $\boldsymbol{k}_{\perp}$, however, is not conserved during the crossing of the surface. The treatment of $\boldsymbol{k}_{\perp}$ is discussed in section 2.2.3.

---

[1] In the experiment, the electron analyser and the sample are in electrical contact, i.e. their Fermi levels are aligned. This means that the work function of the experiment is the analyser work function.

To describe the photoemission process formally, Fermi's golden rule is used to calculate the transition probability w_{fi} from an N-electron initial state $\left|\Psi_i^N\right\rangle$ to an excited final state $\left\langle\Psi_f^N\right|$:

$$w_{fi} = \frac{2\pi}{\hbar}\left|\left\langle\Psi_f^N\middle|H_{\text{int}}\middle|\Psi_i^N\right\rangle\right|^2\delta(E_f^N - E_i^N - h\nu) \tag{2.8}$$

where E_f^N and E_i^N are the final and initial states' energies of the N-electron system. The perturbative Hamiltonian H_{int} describes the photon–electron interaction. As described in Ref. [14, 34], H_{int} can be written as

$$H_{\text{int}} \approx \frac{e}{mc}\boldsymbol{A}\cdot\boldsymbol{p} \tag{2.9}$$

where e and m are the electron's charge and mass, c denotes the speed of light, $\boldsymbol{A}$ is the electromagnetic vector potential and $\boldsymbol{p}$ is the electron momentum operator. As this formalism is within the framework of Fermi's golden rule, it only holds for weak perturbations [38].

From this point, Eq. (2.8) can be further elaborated using different approaches. One is the quantum mechanical approach of the *one-step model* [39], in which the photon absorption, electron excitation and electron detection are treated as a single process. However, this approach is complex and deriving results is difficult. It is therefore more convenient to use the approach of the *three-step model* [40], in which the whole process is divided into the following steps:

1. absorption of the photon, the optical transition
2. propagation of the electron to the surface
3. transmission of the electron through the surface barrier

As illustrated in Fig. 2.10a, in step 1, the information about the intrinsic electronic structure of the material is encoded in the absorption process; this is discussed in more detail below. In step 2, the propagation inside the material is usually described in terms of an effective mean free path λ_{MFP} for the electron, including both elastic and inelastic scattering processes. It has been shown experimentally that this mean free path depends strongly on the kinetic energy but only weakly on the material properties; see Fig. 2.10b. It has a minimum value under 1 nm at 20-100 eV. Generally, for photon energies used in ARPES measurements, the mean free path is on the order of a few Å. This makes measurements, especially in the UV region, highly surface-sensitive, with the signal originating only from the top few atomic layers. Lastly, in step 3, the end state of the electron in vacuum is described as a free-electron plane wave state that extends to the detector, where the kinetic energy and angle of the electron are detected. One has to keep in mind that the three-step

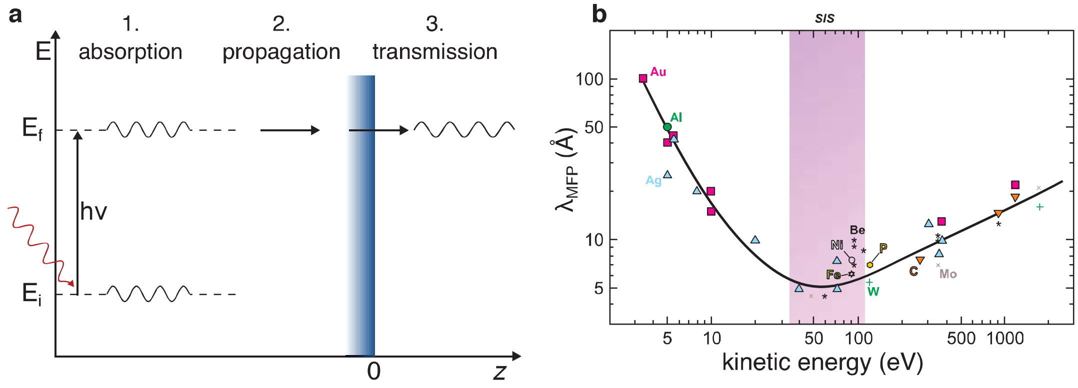

Figure 2.10: Three-step model and inelastic mean free path. **a** Schematic illustration of the three-step model, showing the excitation of an electron from an initial state E_i to a final state E_f, and its propagation to and transmission through the surface. **b** Inelastic mean free path λ_{MFP} as a function of electron kinetic energy for different materials. Adapted from Ref. [41].

model is a simplification that has the advantage of decoupling the different steps, but to fully explain the measured spectral intensities, the one-step model must be used. In the following, the photoemission signal originating from the optical transition is explained within the three-step model framework for both non-interacting and interacting electrons.

Non-Interacting Electrons

In the simplest case, the electrons do not interact and the initial and final states of the first step can be factorized as follows:

$$\left|\Psi_f^N\right\rangle = \mathcal{A}\left|\phi_f^{\boldsymbol{k}}\right\rangle \otimes \left|\Psi_f^{N-1}\right\rangle \tag{2.10}$$

$$\left|\Psi_i^N\right\rangle = \mathcal{A}\left|\phi_i^{\boldsymbol{k}}\right\rangle \otimes \left|\Psi_i^{N-1}\right\rangle \tag{2.11}$$

where $\mathcal{A}$ is an antisymmetry operator that enforces the Pauli principle, and $\left|\phi_i^{\boldsymbol{k}}\right\rangle$ and $\left|\phi_f^{\boldsymbol{k}}\right\rangle$ are the initial and final wave functions of the excited electron with the same wave vector $\boldsymbol{k}$ due to momentum conservation. The electron's energy before and after excitation are denoted as $\epsilon_{\boldsymbol{k}}$ and ϵ_f, and $\left|\Psi_i^{N-1}\right\rangle$ and $\left|\Psi_f^{N-1}\right\rangle$ are the initial and final state wave functions of the remaining $(N-1)$ electron system. Since the electrons are non-interacting, the $(N-1)$-electrons are not affected by the removal of the electron and therefore $\left|\Psi_i^{N-1}\right\rangle = \left|\Psi_f^{N-1}\right\rangle$.

Using Eq. (2.8) and the above approximations, the total photocurrent $I = \sum_{i,f} w_{fi}$

can be calculated as

$$I_{i\to f}(\boldsymbol{k},\epsilon_f) \propto \left|M_{f,i}^{\boldsymbol{k}}\right|^2 \delta(\epsilon_f - \epsilon_{\boldsymbol{k}} - h\nu) \tag{2.12}$$

$$M_{f,i}^{\boldsymbol{k}} \equiv \left\langle \phi_f^{\boldsymbol{k}} \middle| H_{\text{int}} \middle| \phi_i^{\boldsymbol{k}} \right\rangle \tag{2.13}$$

where $M_{f,i}$ is the one-electron dipole matrix element. Here it was assumed that at most a single transition $(i \to f)$ occurs at each $\boldsymbol{k}$.

Eq. (2.12) shows that in ARPES, the spectrum of a non-interacting system has a single peak tracing the electronic band dispersion $\epsilon_{\boldsymbol{k}}$, with its intensity modulated by the dipole matrix element. This illustrates that ARPES is capable of mapping the bands in the material under study. However, in the presence of interactions, this simple picture has to be modified, as described later on.

The dipole matrix element $M_{f,i}^{\boldsymbol{k}}$, as a modulation of the measured intensity, influences the ability of ARPES to extract microscopic information about the initial state. The measurement geometry, together with symmetry or conservation laws, can lead to suppression of certain states in the spectrum. For example, the parity of an electron emitted on a mirror symmetry plane of the sample can be discerned by measuring with different linear light polarizations. Therefore, one can determine the orbital character of bands by making use of the experimental geometry and light polarizations, which is referred to as *linear dichroism*.

Interacting Electrons

If there are interactions between the electrons in the system, one cannot trivially factorize the many-body final and initial states as this was done in the previous section. Nevertheless, Eq. (2.10) and Eq. (2.11) can be used as an approximation under certain conditions, which are explained below.

The removal of the electron can be approximated by an instantaneous process under the *sudden approximation*. This assumes that the photoelectron has a high energy in the final state and that there is no time for it to interact with the $(N-1)$-electron system left behind. This can justify the factorization used in Eq. (2.10). However, the sudden creation of a hole may be accompanied by bosonic excitations like phonons, plasmons and electron–hole pairs. These lead to satellite peaks on the low-energy side of the main photoemission peak.

For the initial state, the interactions can be treated with a mean-field approximation, which allows for the use of Eq. (2.11). The main difference to the non-interacting system lies then in the treatment of the $(N-1)$-electron system, which cannot be regarded as unchanged upon electron removal in the presence of interactions: $\left|\Psi_i^{N-1}\right\rangle \neq \left|\Psi_f^{N-1}\right\rangle$. Instead, the $(N-1)$-electron system can be left in any number of excited states m with eigenfunctions $\left|\Psi_m^{N-1}\right\rangle$ and energies E_m^{N-1}. Therefore, the total transition probability is a sum over all excited states:

$$\sum_{f,i} \left|M_{f,i}^{\boldsymbol{k}}\right|^2 \sum_m \left|\left\langle \Psi_m^{N-1} \middle| \Psi_i^{N-1} \right\rangle\right|^2 \delta(\epsilon_f + E_m^{N-1} - E_i^N - h\nu), \tag{2.14}$$

where $\left|\left\langle \Psi_m^{N-1} \middle| \Psi_i^{N-1} \right\rangle\right|^2$ is the probability that the removal of the electron from state i will leave the $(N-1)$-electron system in the excited state m. In strongly correlated systems, there will be overlaps between many eigenstates, and the spectra will be rich and include satellites and broadened spectral peaks.

Within the Green's function formalism, the single-electron removal spectral function $A^-(\boldsymbol{k}, \omega)$ describes the probability of the remaining $(N-1)$-electron system's energy changing by ω after the removal of an electron with wave vector $\boldsymbol{k}$:

$$A^-(\boldsymbol{k}, \omega) = \sum_m \left|\left\langle \Psi_m^{N-1} \middle| c_{\boldsymbol{k}} \middle| \Psi_i^N \right\rangle\right|^2 \delta(\omega - E_m^{N-1} + E_i^N). \tag{2.15}$$

The full spectral function is then written as $A(\boldsymbol{k}, \omega) = 1/f(\omega) \cdot A^-(\boldsymbol{k}, \omega)$, where $f(\omega)$ is the Fermi–Dirac distribution. This expression can now be used to rewrite Eq. (2.14) as the photoemission intensity:

$$I(\boldsymbol{k}, \omega) = I_0(\boldsymbol{k}, h\nu, \boldsymbol{A}) f(\omega) A(\boldsymbol{k}, \omega). \tag{2.16}$$

This expression represents the photoemission signal under the sudden approximation and in the absence of extrinsic losses, and is proportional to the single-particle spectral function. The Fermi–Dirac distribution ensures that only the occupied electronic states are probed. In practice, ARPES is therefore limited to states below the Fermi level[2]. The prefactor $I_0(\boldsymbol{k}, h\nu, \boldsymbol{A})$ accounts for the intensity modulations associated with the matrix element effects discussed earlier.

The spectral function itself can be expressed in terms of the *proper self-energy* $\Sigma(\boldsymbol{k}, \omega) = \Sigma'(\boldsymbol{k}, \omega) + i\Sigma''(\boldsymbol{k}, \omega)$, which represents the interactions:

$$A(\boldsymbol{k}, \omega) = -\frac{1}{\pi} \frac{\Sigma''(\boldsymbol{k}, \omega)}{[\omega - \epsilon_{\boldsymbol{k}} - \Sigma'(\boldsymbol{k}, \omega)]^2 + [\Sigma''(\boldsymbol{k}, \omega)]^2}. \tag{2.17}$$

From this, it becomes evident that in an ARPES spectrum, the electron band energy $\epsilon_{\boldsymbol{k}}$ is offset by $\Sigma'(\boldsymbol{k}, \omega)$ due to the interactions, while the spectral peak is broadened by $\Sigma''(\boldsymbol{k}, \omega)$. Physically, $\Sigma''(\boldsymbol{k}, \omega)$ represents the lifetime and with this the

---

[2] The unoccupied states can be probed via inverse photoelectron spectroscopy [42].

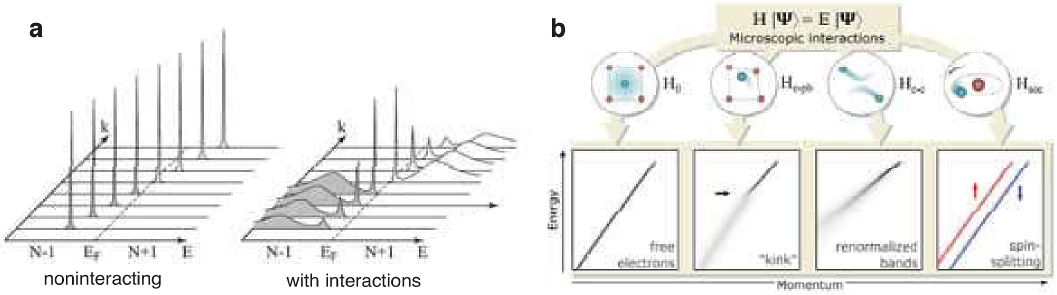

Figure 2.11: Signatures of interactions in the spectral function. **a** Single-electron spectral functions for a non-interacting and interacting electron systems. In the case with interactions, the spectral function shows a quasiparticle peak and an incoherent tail. Adapted from Ref. [43]. **b** Illustration of the effect from different interaction terms (electron–phonon, electron–electron and spin–orbit coupling) on the ARPES spectrum. Adapted from Ref. [14].

energy width of the state. In the non-interacting picture, $\Sigma(\boldsymbol{k},\omega) = 0$ and therefore $A(\boldsymbol{k},\omega) = \delta(\omega - \epsilon_{\boldsymbol{k}})$, consistent with Eq. (2.12).

Finally, for weakly interacting electrons $\Sigma(\boldsymbol{k},\omega)$ can be expanded to first order around $\epsilon_{\boldsymbol{k}}$, which gives

$$A(\boldsymbol{k},\omega) = Z_{\boldsymbol{k}} \frac{\Gamma_{\boldsymbol{k}/\pi}}{(\omega - \epsilon_{\boldsymbol{k}})^2 + \Gamma_{\boldsymbol{k}}^2} + A_{\mathrm{inc}}(\boldsymbol{k},\omega), \tag{2.18}$$

where $Z_{\boldsymbol{k}} = (1 - \partial\Sigma'/\partial\omega)^{-1}$ is the coherence factor, $\epsilon_{\boldsymbol{k}} = Z_{\boldsymbol{k}}(\epsilon_{\boldsymbol{k}} + \Sigma')$ and $\Gamma_{\boldsymbol{k}} = Z_{\boldsymbol{k}}|\Sigma''|$. The self-energy and derivatives are evaluated at $\omega = \epsilon_{\boldsymbol{k}}$. This expression is only valid near the Fermi level and when $|\Sigma''| \ll \epsilon_{\boldsymbol{k}}$ for small ω and $|\boldsymbol{k} - \boldsymbol{k}_F|$. The first term of Eq. (2.18) represents the concept of a quasiparticle according to Fermi liquid theory with a reduced spectral weight $Z_{\boldsymbol{k}}$. The second term A_{inc} is the incoherent part of the spectral function and represents the error introduced by the first-order approximation of $\Sigma(\boldsymbol{k},\omega)$.

In practice, the ARPES spectra show distinct features depending on the kinds of interaction present in the system. This is summarized in Fig. 2.11 for electron–phonon, electron–electron and spin–orbit coupling. The analysis of these features is the starting point for extracting microscopic interactions in various quantum materials.

2.2.2 Technical Requirements

In an ARPES setup, several components must work in concert for a successful measurement. A monochromatic photon beam needs to be focused on the material under study, which needs to have a clean, single-crystalline surface. Then, the photoemitted electrons need to be detected according to their energy and emission angle. For complete control of momenta, the sample orientation requires ideally three translational and three rotational axes. To avoid scattering of the electrons after emission from the sample, the experiment needs to be done in ultra-high vacuum (UHV) conditions below 1×10^{-9} mbar. UHV is also necessary to keep the measured sample surface clean and prevent degradation. Additionally, the sample must be cryogenically cooled to access the exotic phenomena of quantum materials. Like RIXS, an ARPES experiment is a tremendous technical challenge.

In the following, the different parts of the setup – the light source, the sample environment and the detector, which is a photoelectron spectrometer – are introduced, and their properties are discussed as applicable to the scope of this study. The sample preparation is also briefly explained.

Light Source

In an ARPES measurement, the photon energy $h\nu$ defines the photoelectron escape depth, as well as the momentum range that can be probed. As evident from Eq. (2.7), the higher the photon energy, the larger the accessible range of parallel momentum. Therefore, high photon energy sources (e.g. in the high ultraviolet or soft x-ray range) are often chosen for the characterization of new materials to get an overview of the electronic band structure in momentum space. Lower-energy sources, on the other hand, offer better energy and momentum resolution, since $\hbar\Delta\boldsymbol{k}_{\parallel} = \sqrt{2mE_{\mathrm{kin}}}\cos(\theta)\Delta\theta$. The most important factor is that the source must provide a monochromatic photon beam, preferably with a well-defined polarization. In practice, the sources used include lasers, synchrotrons, gas discharge lamps and free-electron lasers. All of these have their own advantages and drawbacks concerning flux, momentum range coverage, energy stability, statistics, energy resolution and beam size among other restricting factors [14]. In this work, the ARPES study employed synchrotron radiation. The working principle and advantages of this type of light source are therefore explained in more detail in the following.

As discussed in section 2.1.2 on the RIXS technical requirements, an undulator insertion device in a synchrotron storage ring provides a well-defined and continuously tunable photon energy as well as control over the polarization. The available polarizations are usually linear horizontal and vertical as well as circular left and right. The beamline for an ARPES endstation usually consists of the same components as for the RIXS endstations; see section 2.1.2. ARPES facilities span the whole range from vacuum ultraviolet (VUV) to hard x-ray wavelengths. However, the majority of experiments are performed in the VUV range, due to the higher cross section and better energy resolution. Measurements in the soft x-ray range are used for bulk measurements and the dependence of the perpendicular momentum in three-dimensional materials, since the electronic mean free path is higher for higher photon energies and therefore the bulk sensitivity is enhanced.

The continuously tunable photon energy allows for a $\boldsymbol{k}_{\perp}$ mapping and the identification of two-dimensional surface states. Additionally, the photon energy can be tuned to resonances to enhance certain features in the band structure. The full control over the polarization enables studies of the bands' orbital character via the linear dichroism. Another advantage of synchrotron radiation is its high flux and coherence. However, these advantages come at the cost of energy resolution and the organizational complications of operating at a large-scale synchrotron facility, where measurement time is extremely restricted and only the strongest proposals get accepted for beamtime. The ARPES data presented in this work were collected at the Surface/Interface Spectroscopy Ultra Low-Temperature High-Resolution (SIS ULTRA) ARPES endstation at the Swiss Light Source. This beamline provides photon energies from 20 to 800 eV and linear and circular polarization control.

Sample Environment

To resolve the momentum of the photoelectrons reaching the detector, the geometry between the light source, the sample lattice orientation and the detector needs to be well defined and controlled. As with RIXS experiments, the sample in an ARPES measurement is mounted on a manipulator with rotational and translational degrees of freedom. At the SIS beamline, a six-axis manipulator is used, enabling control of (x, y, z) translational and $(\theta, \mathrm{tilt}, \phi)$ rotational degrees of freedom. The sample is cooled by a helium flow cryostat in the manipulator. The manipulator can operate from room temperature down to 4 K [44]. Another vital aspect is the magnetic shielding. The electron's trajectory in vacuum needs to be preserved until it reaches the detector for original momentum to be determined precisely. Therefore, the magnetic field must be below $\leq 100\,\mathrm{nT}$ at the measurement position. As mentioned above, the preservation of the electron's trajectory also requires UHV conditions to minimize scattering events and degradation of the surface. Since only the topmost layer of the material contributes to the signal in this extremely surface-sensitive technique, even small variations of the material surface, like surface oxidation or adhesion of atmospheric molecules, can have a deleterious impact on the measurement.

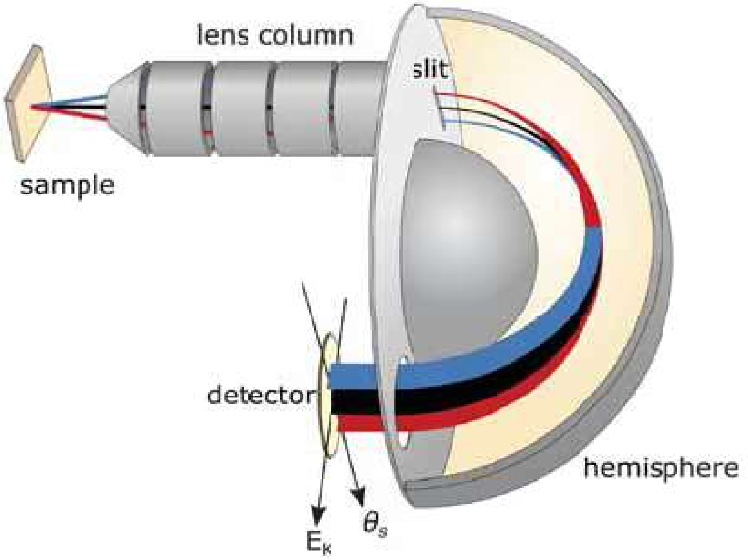

Figure 2.12: Hemispherical photoelectron analyser. The electrons escaping from the sample first pass the lens column, which maps the angular distribution onto the entrance slit of the analyser. Between the hemispherical shells, the electrons get dispersed according to their energy and are then recorded on a two-dimensional detector according to their angular and kinetic energy distributions. Adapted from Ref. [14].

Photoelectron Spectrometer

To infer the energy–momentum state of emitted electrons, they must be detected energy and angle-resolved. To achieve this, a photoelectron spectrometer consists of electrostatic elements to focus and disperse the electrons according to their energy before detecting them while maintaining their angular distribution. Nowadays, several different photoelectron energy analysers are available, including hemispherical analysers, time-of-flight spectrometers and momentum microscopes [14]. The SIS ARPES endstation employed in this work uses a hemispherical analyser (Scienta Omicron DA30-L [45]), and this type of detector is therefore explained here.

A schematic illustration of a hemispherical analyser is shown in Fig. 2.12, with its important components: the input lens column, the hemispherical shells and a two-dimensional electron detector. After escaping the sample surface, photoelectrons within a finite acceptance angle enter the spectrometer and pass through the lens column, where they are focused and their angular distribution is imaged onto the entrance slit of the hemispherical analyser. The main part of the analyser consists of two concentric hemispherical electrode shells, between which an electrostatic potential difference (the pass energy E_{pass}) is applied. This creates a radial electric field between the shells, and the electrons passing through are deflected towards the inner sphere with a radius defined by the applied potential E_{pass} and their respective kinetic energy at the moment they enter through the slit. This means that electrons with different kinetic energies are dispersed along the radial direction of the hemisphere, arriving at different radial positions on the detector. The electrons enter through the slit with different emission angles along the slit direction, which are mapped on the detector to different orthogonal positions. Thus, the detector records the two-dimensional photoelectron intensity with respect to the emission angle θ_s and the kinetic energy E_k. The acceptance angles are typically ± 15°, or ± 7° in the high angular resolution mode. To map the angles perpendicular to the slit direction, the sample is usually rotated about the axis parallel to the slit. Some detectors have nowadays a deflection mode, which allows for the collection of photoelectrons with different angles perpendicular to θ_s. This allows for mapping perpendicular to the slit direction without rotating the sample. The two-dimensional electron detector itself consists of a multichannel plate that amplifies the signal, in front of a phosphor screen from which the luminescence image can be read using a CCD camera.

Sample Preparation

As highlighted above, ARPES is an extremely surface-sensitive technique, with only the topmost layers of the material contributing to the signal. Therefore, the measured surface of a single-crystalline sample needs to be extremely flat and clean. To create a sufficiently clean surface, different approaches can be used. One is the previously described *top-post cleaving method*; see section 2.1.2 under "Sample Preparation". This method is routinely used for single-crystalline bulk samples that are layered – i.e. that have a strong degree of two-dimensionality, offering a natural cleaving plane along the layers.

Another approach is connected to thin film samples, which are grown in situ under UHV to prevent any source of contamination. Different preparation techniques exist, but the growth technique adopted in this study is pulsed laser deposition (PLD) [46]. Thin films are prepared by using a focused pulsed-laser beam to ablate from a target. For this, elementary or alloy targets are placed in a UHV chamber and struck by the pulsed laser beam, as illustrated in Fig. 2.13a. The beam ablates atoms and ions from the target, creating a plasma plume in front of the target. Close to the target, there is the substrate on which the film is grown, and the particles in the plume are deposited on its surface. Usually, the substrates are placed with the surface parallel to the target surface at a distance of a few centimeters. After deposition, the substrate with the film on it is annealed to achieve a flat and ordered surface. For successful PLD growth, many parameters must be adjusted for each specific material, including laser parameters like fluence, wavelength, pulse duration and

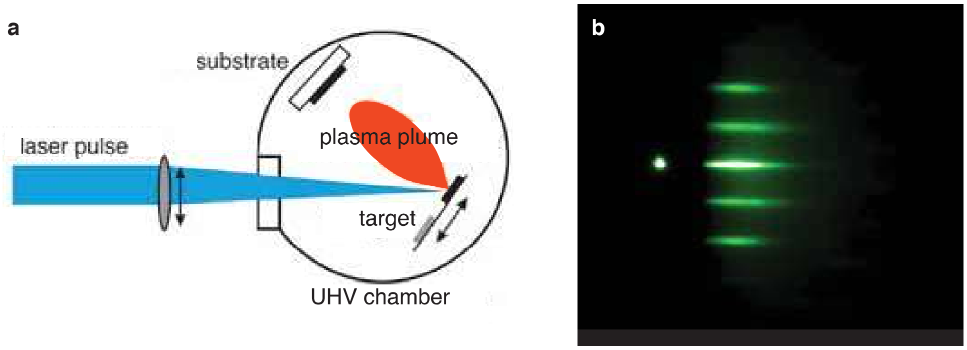

Figure 2.13: PLD growth and RHEED pattern. **a** Illustration of the PLD setup and growth process. Adapted from Ref. [46]. **b** Example RHEED pattern after the thin film growth.

repetition rate, as well as the target-to-substrate distance, substrate temperature and background gas and pressure.

During and after the growth, the surface quality of the thin film is monitored using reflection high-energy electron diffraction (RHEED). High-energy electrons strike the surface at a small grazing angle and are diffracted from the atoms on the surface. The interference pattern of the electrons is then detected by a photoluminescent screen. By analysing the interference patten, the crystallography of the sample surface can be investigated. For a two-dimensional, flat thin film, the diffraction pattern consists of equidistant parallel lines, with their distance defined by the periodicity of the surface lattice. Such a RHEED pattern is shown in Fig. 2.13b. Since the intensities of the lines fluctuate periodically as a result of the relative surface coverage, the growth can be monitored layer by layer.

2.2.3 Data Analysis

After the experiment, the raw data collected from the detector image need to be processed to extract information about the electronic band structure. As described above, the raw data is a two-dimensional array of intensities as a function of the kinetic energy E_k and the slit angle θ_s. The goal is to extract the spectral intensity as a function of the binding energy E_B and the momentum wave vector $\boldsymbol{k}$, therefore, two conversions need to be performed: kinetic energy to binding energy and angle to momentum. The two steps are briefly explained below. Furthermore, the process of extracting one- or two-dimensional spectra for a quantitative analysis is outlined.

Energy Level Adjustment

To convert the kinetic energy E_k measured at the detector to the intrinsic binding energy E_B with respect to the Fermi level E_F of the electrons inside the material, a rigid shift of $\Phi_A - h\nu$, where Φ_A is the analyser work function, is applied to the energy axis of the spectrum. However, due to the uncertainty in the work function and distortions from the slit geometry, it is more accurate to determine E_F by fitting a Fermi–Dirac distribution to the spectrum of a reference material, e.g. a polycrystalline metal in electrical and thermal contact with the sample (to ensure the same E_F as the sample), or to the measured spectrum itself. For the reference measurement, it has to be ensured that the scan is repeated with identical parameters as used for the actual measurement on the sample. Since the reference metal is polycrystalline, there is no angular variation in the spectral weight and an isotropic distribution is expected below E_F. Therefore, the position of E_F can be extracted for each angular channel of the detector image by extracting the intensity as a function of energy at that channel and fitting the spectrum to the a Fermi–Dirac distribution for the corresponding temperature. To incorporate the broadening due to the finite energy resolution of the experiment, the Fermi–Dirac distribution is convolved with a Gaussian distribution, whose standard deviation σ represents the overall instrumental energy resolution in the given experiment. Additionally, inelastic scattering processes lead to an increasing background below the Fermi level, which can be incorporated into the fit by assuming a linear slope below E_F. Altogether, the fit function used to determine the Fermi level for a given spectrum is

$$\mathrm{fit}(E, E_F, T, \sigma, a) = (f * g)(E, E_F, T, \sigma) + \Theta(E - E_F) \cdot a \cdot e \tag{2.19}$$

where

$$f(E, E_F, T) = (\exp[(E - E_F)/(k_B T)] + 1)^{-1} \tag{2.20}$$

$$g(E, \sigma) = \exp\left[-1/2 \cdot (E/\sigma)^2\right] \tag{2.21}$$

$$\Theta(E - E_F) = \begin{cases} 0, & \text{if } E > E_F \\ 1, & \text{otherwise} \end{cases} \tag{2.22}$$

and k_B is the Boltzmann constant. From this fit, the Fermi level for each angular detector channel can be determined. Since this E_F distribution contains some noise due to uncertainty, it is fitted by a polynomial. The now continuous Fermi levels obtained from the polynomial fit are used to correct the energy scale in the spectrum for each channel.

Angle to Momentum Conversion

To convert the experimental angular orientation of the measured photoelectrons to their preemission momentum inside the crystal lattice, both the absolute value and direction of the momentum need to be defined. The ultimate goal is to calculate all three momentum components (k_x, k_y, k_z) within the sample's crystal axis coordinate system. From Eq. (2.6), the kinetic energy after absorption of the photon, and with this the absolute momentum value, can be calculated:

$$k = \frac{\sqrt{2m}}{\hbar}\sqrt{h\nu - \Phi - E_B}. \tag{2.23}$$

As mentioned above, however, only the parallel component $k_\parallel$ is conserved upon crossing the surface in the third step of the three-step model. Nonetheless, the effect of passing through the surface can be modelled by an inner potential V_0 inside the crystal, which drops to zero at the sample surface. The electron passing the surface therefore has to overcome this potential difference, which affects only its perpendicular momentum component; see Fig. 2.9b. Energetically, V_0 corresponds to the energy of the bottom of the valence band referenced to the vacuum level [34]. The momentum components $(k_\perp, k_\parallel)$ of the photoelectron inside the crystal can thus be calculated from the momentum in vacuum $(k_{\perp,0}, k_{\parallel,0})$ as

$$k_\parallel = k_{\parallel,0}, \tag{2.24}$$

$$k_\perp = \sqrt{k_{\perp,0}^2 + \frac{2mV_0}{\hbar^2}}. \tag{2.25}$$

The inner potential V_0 can be seen as the average effective potential experienced by the electrons inside the crystal. It is *a priori* not known but can be used as a fitting parameter in the $k_\perp$ momentum periodicity.

To calculate the full orientation within the sample's coordination system, the whole experimental geometry needs to be taken into account. From the experimental data, one dimension of the two-dimensional detector output is the slit angle θ_s. This defines the momentum vector of the photoelectron within the lab frame. To transform this into the sample frame, the relative orientation of the detector slit towards the sample's crystal lattice axes needs to be taken into account. In practice, there are two different geometries commonly used in an ARPES setup: the *horizontal* geometry, in which the analyser slit lies within the experimental mirror plane defined by the incoming photon $\boldsymbol{k}_{h\nu,in}$ and the outgoing photoelectron with wave vector $\boldsymbol{k}_{e^-,out}$; and the vertical geometry, in which the analyser slit is perpendicular to the mirror plane. Thus, the slit geometry together with the slit angle θ_s allows for the determination of the momentum in the lab frame.

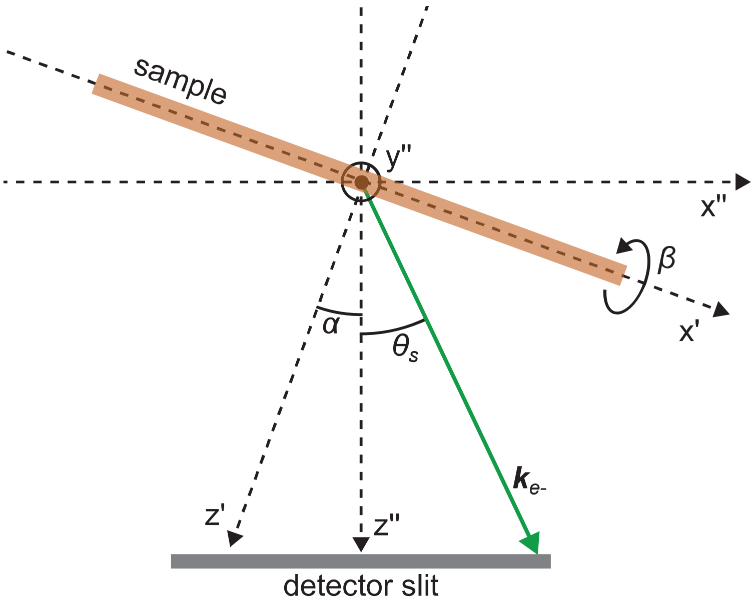

Figure 2.14: Experimental geometry. Schematic of the experimental geometry with a horizontal slit arrangement. The coordinate system of the lab frame is denoted with x'', y'' and z''. The sample is first rotated around the fixed axis y'' by an angle α, introducing the rotated coordinate system x' and z'. The sample is then rotated around the new x'-axis by an angle β. The photoelectron momentum $\boldsymbol{k}_{e-}$ in the lab frame is translated to the coordinate system of the sample to infer the intrinsic momentum.

For the conversion into the sample frame, the orientation of the sample with respect to the mirror plane needs to be taken into account. Usually, the sample is mounted on a manipulator with three rotational degrees of freedom; see section 2.1.2 under "Sample Environment". As depicted in Fig. 2.14 for the horizontal slit arrangement, the sample is rotated first by an angle α around the fixed, independent lab frame rotation axis y'', which is the manipulator axis perpendicular to the mirror plane. This creates an intermediate reference frame (x', y', z'). The sample can then be rotated by an angle β around the x'-axis. In the horizontal slit geometry, this is the rotation performed to record a k-space map. As a third rotation, the sample can be rotated by an angle γ around the current z axis, which is often called the *azimuth* rotation. However, this rotation corresponds to the k-space rotations about the same angle, which means that it is independent and can be applied as a final step. Altogether, the momentum (k_x, k_y, k_z) is determined by calculating back from the lab frame to the sample frame, taking the first two rotations (α and β) into account.

For the horizontal slit arrangment, in which the analyser slit lies in the $x''z''$-plane, the three momentum components are given by

$$k_x = k \cdot \underbrace{\sin(\alpha + \theta_s)}_{\text{projection on } x'} \tag{2.26}$$

$$\begin{aligned} k_y &= k \cdot \underbrace{\cos(\alpha + \theta_s)}_{\text{projection on } z'} \cdot \underbrace{\cos(90 - \beta)}_{\text{projection on } y} \\ &= k \cdot \cos(\alpha + \theta_s) \cdot \sin(\beta) \end{aligned} \tag{2.27}$$

$$k_{z,0} = k \cdot \underbrace{\cos(\alpha + \theta_s)}_{\text{projection on } z'} \cdot \underbrace{\cos(\beta)}_{\text{projection on } z} \tag{2.28}$$

$$k_z = \sqrt{k_{z,0}^2 + \frac{2mV_0}{\hbar^2}} \tag{2.29}$$

where k is given by Eq. (2.23).

For the vertical slit arrangement, in which the analyser slit lies in the $y''z''$-plane, the three momentum components are given by

$$k_x = k \cdot \underbrace{\cos(\theta_s)}_{\text{projection on } z''} \cdot \underbrace{\sin(\alpha)}_{\text{projection on } x'} \tag{2.30}$$

$$k_y = k \left[\underbrace{\cos(\theta_s)}_{\text{projection on } z''} \cdot \underbrace{\cos(\alpha)}_{\text{projection on } z'} \cdot \underbrace{\sin(\beta)}_{\text{projection on } y} + \underbrace{\sin(\theta_s)}_{\text{projection on } y''} \cdot \underbrace{\cos(\beta)}_{\text{projection on } y} \right] \tag{2.31}$$

$$k_{z,0} = k \left[\underbrace{\cos(\theta_s)}_{\text{projection on } z''} \cdot \underbrace{\cos(\alpha)}_{\text{projection on } z'} \cdot \underbrace{\cos(\beta)}_{\text{projection on } z} + \underbrace{\sin(\theta_s)}_{\text{projection on } y''} \cdot \underbrace{\sin(\beta)}_{\text{projection on } z} \right] \tag{2.32}$$

$$k_z = \sqrt{k_{z,0}^2 + \frac{2mV_0}{\hbar^2}} \tag{2.33}$$

A more detailed discussion with a slightly different approach can be found in Ref. [36]. As discussed above, the azimuth rotation γ can be applied as a last step, since there is a correspondence between real and reciprocal space rotation. This means that, no matter in which frame, γ always corresponds to a rotation around the *current* z-axis. Therefore, the converted $\boldsymbol{k} = (k_x, k_y, k_z)$ can simply be multiplied by $R_z(\gamma)$, where R_z is the three-dimensional rotation matrix around the z-axis.

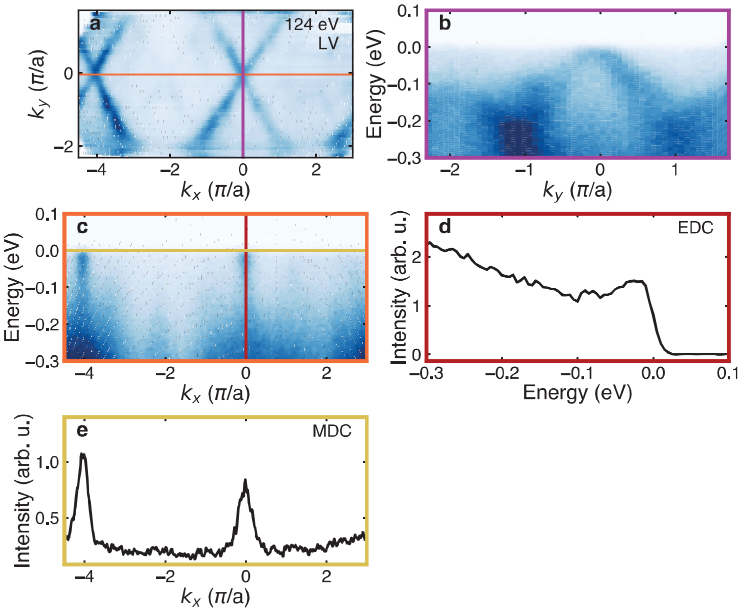

Figure 2.15: Data extraction and plotting. **a** Two-dimensional Fermi surface map. Solid lines indicate the cuts to extract the energy distribution maps in **b, c**. Solid lines in **c** indicate the cuts where the energy and momentum distribution curves in **d, e** have been extracted, respectively.

Three-, Two- and One-Dimensional Spectrum Extraction

As explained, modern photoelectron analysers provide as output data a two-dimensional intensity map as a function of energy and slit angle, or k_x momentum after conversion. To obtain a constant energy surface, like the Fermi surface, as a function of in-plane momenta k_x and k_y, the sample is rotated by the axis parallel to the detector slit. Like this, the dataset becomes three-dimensional: photoelectron intensities as a function of energy, k_x and k_y. Extraction of the Fermi surface is done by choosing the intensities for each k_x and k_y at the Fermi energy, usually by interpolation and integration in a small energy window around E_F. Such a Fermi surface is shown in Fig. 2.15a, for the heavy fermion compound $PrFe_4P_{12}$.

From the three-dimensional dataset, one can now also extract energy distribution maps at different k_x or k_y values, as shown in Fig. 2.15b and c. These maps illustrate the band dispersion along an in-plane momentum direction.

To extract quantitative information about the band structure and intrinsic correlations via the spectral function, one-dimensional spectra of the intensity versus momentum or energy are extracted from the energy distribution maps. These spectra are known as energy distribution curves (EDCs) or momentum distribution curves (MDCs). Examples are shown in Fig. 2.15d and e, respectively. From these, the band dispersion can approximately be obtained by fitting the intensity peak of an MDC or EDC. However, due to the energy and momentum dependence of the self-energy and the matrix element, the peak positions obtained from an MDC or EDC are not identical. Usually, it is assumed that the self-energy is momentum-independent, simplifying Eq. (2.17). Then, the electronic band in the MDC curves assumes a Lorentzian lineshape whose peak position represents the band energy ϵ_k.

3 Low-Energy Orbital Texture of Calcium Ruthenates

The first group of quantum materials discussed in this work are the calcium ruthenates, which are an excellent example of how the interplay between different degrees of freedom can lead to a wealth of macroscopic phenomena. In order to shed light on the microscopic mechanisms behind these phenomena, many different experimental and theoretical approaches need to be combined. This chapter, however, focuses on the work that has been done employing resonant inelastic x-ray scattering and is based mainly on two manuscripts: "Resonant inelastic x-ray scattering study of $Ca_3Ru_2O_7$" (section 3.3) and "Resolving the Orbital Character of Low-energy Excitations in Mott Insulator with Intermediate Spin-orbit Coupling" (section 3.4). The first manuscript has been published in a peer-reviewed journal [47], whereas the second has recently been submitted [48]. My contributions as the first author of the first manuscript include the entirety of the data analysis. For the second manuscript, my contribution includes planning, preparing and executing the experiments, and leading and assisting a master's student, Pascal Rothenbühler, through the data analysis. For both manuscripts, I took the lead in manuscript preparation and discussions with the theorists Mario Cuoco and Fiona Forte, who developed the calculations and theoretical interpretations. Before discussing the findings of these two manuscripts, the ruthenates and their relevant energy scales are described, and the early RIXS measurements are summarized.

3.1 Calcium Ruthenates and Their Relevant Energy Scales

In the zoo of quantum materials, a group intensively studied is the $3d$ and $4d$ transition metal oxides (TMOs), in which strong electronic correlations dominate the microscopic interactions. Compared to $3d$ TMOs, $4d$ TMOs have larger bandwidths due to the more extended $4d$ orbitals. This leads to the electrons having a combination of itinerant and localized properties, resulting in a wealth of fascinating phenomena and an intricate interplay of different energy scales. This makes $4d$ TMO particularly complex and to understand their properties, one has to take into account several different degrees of freedom: the lattice, charge, spin and orbital degrees of freedom as well as their local interactions. First, the crystal field splitting describes the splitting of the $4d$ energy levels due to the structural environment of the transition metal. Next are the interatomic Coulomb interaction and the spin–orbit coupling. Last, the Hund's coupling needs to be taken into account: this is the energy scale associated with intra-atomic exchange. It lowers the repulsive Coulomb energy cost when placing two electrons in different orbitals with parallel spin, as opposed to placing them in the same orbital. In the $4d$ TMOs, all these energy scales are comparable, which leads to constant competition and means that small perturbations can have a large impact on the physical properties of these materials. For example, an intensively studied phenomenon is the metal-to-insulator transition. For strong Coulomb repulsion and reduced bandwidth, the electrons become localized and the system enters a Mott insulating state [49, 50]. However, superconductivity and colossal magnetoresistance can also be found in these materials [51, 52].

Most intriguing are the multiband systems that display strong correlations while not necessarily being close to a Mott insulating state. In these materials, the Hund's coupling adds an additional channel for strong correlations. In Fig. 3.1a, the degree of correlation for a three-orbital model with partially filled t_{2g} shells is shown. The quasiparticle weight Z is plotted as a function of the number of electrons per site n, i.e. the band filling, versus the Coulomb interaction U normalized to the halfbandwidth D. The model considers a fixed Hund's coupling of $0.15\,U$. Darker regions ($Z \approx 1$) correspond to good metals, while lighter regions ($Z \approx 0$) correspond to correlated metals. At half filling, there is a stabilized Mott insulating state, depicted by the black vertical bar. Interestingly, to the left and right of half filling, i.e. for 2 or 4 electrons per site, there is a large region where the quasiparticle weight is essentially zero and correlated behaviour is displayed, but the Mott insulating state is still not established. There, the Hund's coupling drives the system away from the Mott transition, but the metallic state is more correlated due to a lowered quasiparticle coherence [53]. The Hund's coupling acts as an additional channel for strong correlations. Apart from Hund's coupling, the problem is further complicated by strong spin–orbit coupling, as the various degrees of freedom, including charge, spin and orbital, cannot be treated individually and a new conceptual framework needs to be adopted compared to $3d$ systems.

One of the material families that lies in the border region between the Mott insulating state and the strongly correlated metallic phases is the ruthenates. The Ruddlesden–Popper series compounds have the form $(\mathrm{Sr,Ca})_{n+1}\mathrm{Ru}_n\mathrm{O}_{3n+1}$, where n layers of the perovskite lattice RuO_3 are interleaved by a spacer layer. In the perovskite lattice,

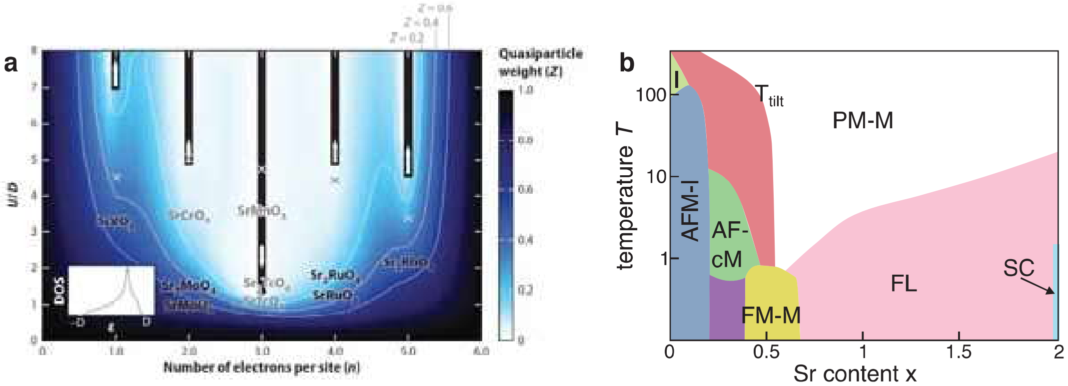

Figure 3.1: Correlations and the ruthenates a Degree of correlations (quasiparticle weight Z) of TMO with a partially filled t_{2g} shell as a function of the interaction strength U, normalized by the half-bandwidth D, and the number of electrons per site. Black bars indicate the Mott insulating phases ($U > U_c$) and the white arrows show the evolution of U_c upon further increasing the Hund's coupling. From Ref. [53]. **b** Phase diagram of $Ca_{2-x}Sr_xRuO_4$ as a function of Sr for Ca substitution, showing a wide range of phases including Fermi liquid (FL), antiferromagnetic (AFM) insulator (I), ferromagnetic (FM) metal (M), paramagnetic metal (PM-M), correlated metal (cM) and superconductivity (SC). Adapted from Ref. [10].

the octahedral crystal field environment of the transition metal lifts the degeneracy of the Ru d orbitals. At lower energy lie the t_{2g} states composed of d_{xy}, d_{xz} and d_{yz} orbitals, whereas the e_g orbitals, d_{z^2} and $d_{x^2-y^2}$, are raised to higher energy [54]. The Ru valence states in the t_{2g} orbitals are occupied by 4 electrons, resulting in a multiband system with 2/3 occupancy.

Figure 3.1b depicts the rich phase diagram of the single-layer series as a function of isovalent substitution of Ca with Sr. There is a wealth of different phases and the system goes from an unconventional superconductor on the Sr side all the way to a Mott insulating state on the Ca side. In between are numerous magnetic order and metallic states, highlighting the intricate interplay of the different energy scales present in this system and demonstrating the high tunability of the physical properties. In order to understand the microscopic physics, knowledge of the electronic structure, the structural distortions as well as the orbital and spin–orbital interactions is vital. Therefore, a great deal of effort has been put into the study of these systems, focusing on the ruthenium bands responsible for strong correlations and magnetic interactions. This work focuses on the Ca ruthenates, whose phase diagram displays the metal-to-insulator transition for the single layer. Instead of chemical substitution as a tuning parameter, this work studies the change in dimensionality, comparing the quasi-two-dimensional single layer to the bilayer compound, in which out-of-plane interactions start to play a role. A focus of the investigation is on how the different macroscopic physical behaviours are imprinted in the low energy scales, defined by

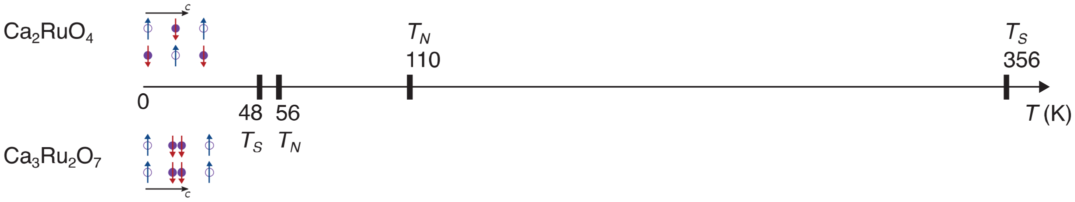

Figure 3.2: Transitions in Ca_2RuO_4 and $Ca_3Ru_2O_7$. Structural (T_S) and magnetic (T_N) transitions in Ca_2RuO_4 and $Ca_3Ru_2O_7$ are indicated on a temperature axis. Coloured symbold depict the antiferromagnetic order below the magnetic transitions for both compounds.

structural and spin–orbital interactions. Below, the two compounds, Ca_2RuO_4 and $Ca_3Ru_2O_7$ and their physical properties are briefly introduced.

3.1.1 Band–Mott Insulator Ca_2RuO_4

The single-layer perovskite compound Ca_2RuO_4 is known for its long-debated metal-to-insulator transition. At $T_S = 356\,\mathrm{K}$, the compound undergoes a first-order structural transition, which compresses the c-axis lattice parameter by around 1.2% [55] and causes the system to become insulating; see Fig. 3.2. This transition was referred to as a Mott transition early on, attributed to the increased ratio of Coulomb interaction to bandwidth [56]. However, due to the multiband structure, both Mott and band insulating mechanisms are involved. It could be shown that the c-axis compression lowers the energy level of the d_{xy} orbital relative to the d_{xz} and d_{yz} orbitals, which leaves the d_{xy} orbital almost fully occupied and therefore band insulating [16]. The Mott gap then opens in the half-filled d_{xz} and d_{yz} bands, completing the band–Mott insulating transition. Below this transition, Ca_2RuO_4 is a paramagnetic insulator, before it undergoes a magnetic transition to a G-type antiferromagnetic (AFM) ordered phase at $T_N = 110\,\mathrm{K}$ [57], in which the magnetic moments are antiferromagnetically aligned both in- and out-of-plane; see inset of Fig. 3.2. At low temperatures, Ca_2RuO_4 has lattice constants $a = 5.39\,\text{Å}$, $b = 5.63\,\text{Å}$ and $c = 11.75\,\text{Å}$ and shows distortions in the form of a rotation and tilt of the RuO_6 octahedra compared to the undistorted crystal structure of Sr_2RuO_4 [57]; see Fig. 3.3a. Both distortions are caused by the smaller ionic radius of Ca compared to Sr, which leads to a reduction of the hopping matrix element and thus enhances correlation effects.

In addition to the metal-to-insulator transition, superconductivity has been reported in thin films [58] or upon application of hydrostatic pressure [59]. Furthermore, both phase and amplitude spin excitation modes consistent with a spin–orbit exciton have been reported by neutron and Raman scattering experiments [60, 61].

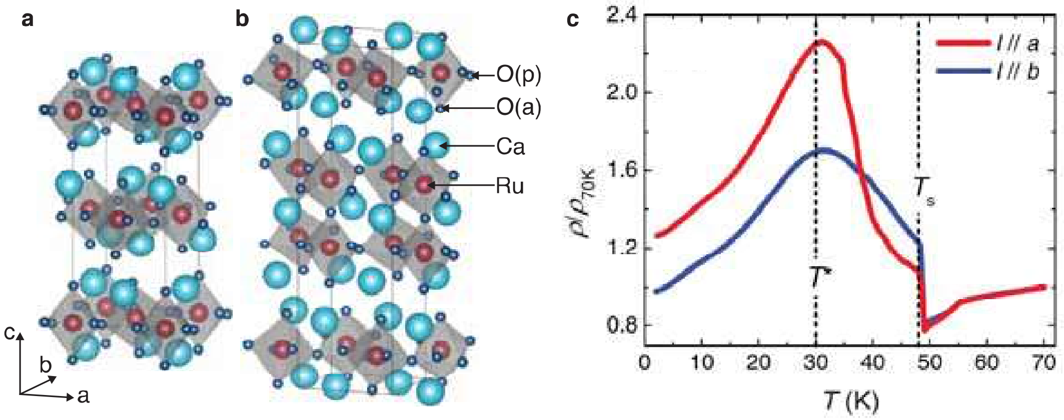

Figure 3.3: Ca_2RuO_4 and $Ca_3Ru_2O_7$. **a** Crystal structure of Ca_2RuO_4. **b** Crystal structure of $Ca_3Ru_2O_7$. The different oxygen sites are indicated as O(p) for the planar site and O(a) for the apical site. **c** Normalized resistivity as a function of temperature for $Ca_3Ru_2O_7$ along *a*- and *b*-axes as indicated. From Ref. [62].

3.1.2 Semimetallic $Ca_3Ru_2O_7$

The next compound in the Ruddlesden–Popper series is the bilayer $Ca_3Ru_2O_7$ and the addition of another perovskite layer changes the physical properties significantly. Upon cooling, $Ca_3Ru_2O_7$ first undergoes a magnetic transition at $T_N = 56\,\mathrm{K}$ to an A-type AFM state, in which the in-plane magnetic moments are aligned ferromagnetically, as opposed to Ca_2RuO_4, and only in the out-of-plane direction are the moments aligned antiferrmagnetic between the double layers; see inset of Fig. 3.2 [63]. As in Ca_2RuO_4, there is also a first-order structural transition in $Ca_3Ru_2O_7$, but only upon further cooling down to $T_S = 48\,\mathrm{K}$. Initially, this transition was, analogously to Ca_2RuO_4, referred to as a metal–insulator transition [64, 65, 66], but the system does not become fully insulating and remains semimetallic down to the lowest temperatures. However, the resistivity is highly anisotropic, not only between in- and out-of-plane directions, but also within the in-plane directions; see Fig. 3.3c. In fact, the resistivity along the *a*- and *b*-axes shows a distinct difference below the structural transition temperature. Even more intriguing, the data suggest an additional transition at $T = 30\,\mathrm{K}$, where a partial gap opening has been suggested [62]. A full understanding of these phenomena is, however, still lacking. Quantum oscillation experiments observed the quasi-two-dimensional metallicity at low temperatures, which emerge from small Fermi surface pockets [67, 68]. In contrast to this, ARPES measurements have been reported that suggest boomerang-like Fermi arcs [69].

However, the structural transtion at $T = 48\,\mathrm{K}$ in $Ca_3Ru_2O_7$ shows similarities to that in Ca_2RuO_4, even though it is not a full Mott transition. The lattice response shows a *c*-axis lattice parameter compression of around 0.1% [63]. At low temperatures,

$Ca_3Ru_2O_7$ has lattice parameters $a = 5.37\,\text{Å}$, $b = 5.54\,\text{Å}$ and $c = 19.52\,\text{Å}$, and shows the rotation and tilt of the RuO_6 octahedra; see Fig. 3.3b.

Apart from the phenomena mentioned above, $Ca_3Ru_2O_7$ shows colossal magnetoresistance [68, 70], and the Mott insulating state can be recovered by Ti doping, whereas the magnetic structure transforms from A-type to G-type AFM [65]. Most intriguing, the Mott insulating state in Ti-doped $Ca_3Ru_2O_7$ collapses upon application of a modest magnetic field, and a negative colossal magnetoresistance is observed instead.

3.2 Early RIXS Measurements

After the discovery of the unusual physical properties of Ca ruthenates, it became clear that an understanding of these phenomena can only be reached by studying the low-energy microscopic energy scales, like crystal-field splitting, Hund's- and spin–orbit coupling. In Ca ruthenates, these energy scales are comparable in magnitude and, therefore, there is a constant competition leading to high tunability. The direct measurements of these energy scales is, however, extremely challenging, since they are often intertwined and only detectable through second-order effects. One measurement technique that has been successfully applied to this class of materials is RIXS, which was introduced in the previous chapter. There, the energy scales are accessed by measureing the low-energy excitation spectrum, which is a direct fingerprint of the split levels due to the different energy scales.

An early RIXS study by C. Fatuzzo *et al.* [71] reports RIXS measurements at the oxygen K-edge on Sr_2RuO_4 and Ca_2RuO_4, where the ruthenium $4d$ orbitals are accessed through their hybridization with oxygen p orbitals. The absorption spectra confirm an almost fully occupied ruthenium d_{xy} orbital and the RIXS spectra reveal, in addition to the higher-energy dd excitations between the t_{2g} and e_g levels, a low-energy excitation at $\approx 350\,\text{meV}$ consistent with an orbital excitation of the crystal-field and spin–orbit coupling split t_{2g} energy levels; see Fig. 3.4a. A minimal model estimates the spin–orbit coupling to be $\approx 200\,\text{meV}$.

A later study by L. Das *et al.* [72] followed up on these results and published a detailed XAS and RIXS study of Ca_2RuO_4. It revealed a series of excitations in Ca_2RuO_4 within the t_{2g} subspace, consisting of two low-energy and two mid-energy structures; see Fig. 3.4b. The low-energy excitations, around 80 meV and 350 meV, were ascribed to composite spin–orbital excitations determined by the relative strength of the crystal-field splitting and spin–orbit coupling. The mid-energy excitations, at around 1.3 eV and 2.2 eV, correspond to intra-atomic singlet–triplet excitations at an energy

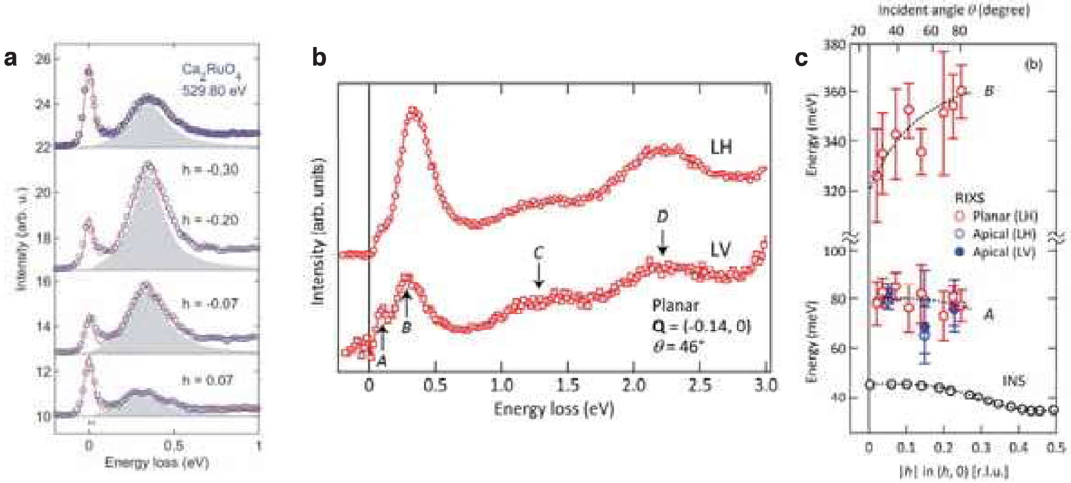

Figure 3.4: Early RIXS measurements on Ca_2RuO_4. **a** Low-energy part of the RIXS spectra for different in-plane momentum transfers h as indicated, showing a clear excitation at $\approx$ 350 meV. From Ref. [71]. **b** Newer low-energy part of the RIXS spectra recorded with different light polarizations as indicated and with elastic scattering subtracted. Four distinct excitations are labelled A-D. **c** Dispersion extracted from excitations A and B in **b** as well as the spin excitation observed with neutron scattering. From Ref. [72].

set by the Hund's coupling and Coulomb interaction. Theoretical calculation of these RIXS spectra, by modelling a cluster of two ruthenium sites connected by one planar oxygen site, related the data to a microscopic physical picture and allowed for an estimation of the relative strength of crystal-field splitting and spin–orbit coupling, and therefore an estimation of all relevant energy scales. The values adopted in the study are a Coulomb interaction of 2 eV, a Hund's coupling of 0.5 eV, a crystal-field splitting of 0.3 eV and a spin–orbit coupling of 0.075 eV. However, the value of the spin–orbit coupling is imprinted in the fine structure of the 350 meV excitation sector, where it leads to a splitting of this sector into four distinct energy levels. This fine structure, as well as a magnetic excitation predicted by the model at around 40 meV, could not be directly resolved due to limitations in energy resolution. For the low-energy excitation detected at 350 meV, the dependence of the excitation energy on the in-plane momentum transfer h revealed a clear dispersion, indicative of the propagating nature of this spin–orbital excitation. In summary, the study showed that spin–orbit coupling is crucial to explaining the nature of these excitations.

Recently, RIXS spectra have been measured at the ruthenium L_3-edge, which directly accesses the ruthenium d orbitals. This was previously not possible, since the excitation energy of $\sim$ 2.8-3 keV lies in the tender x-ray region [73], where the wavelength is too large to match the inter-plane spacing in hard x-ray crystal monochromators but too small for the grooves of grating monochromators used for soft x-rays. This technical difficulty has been overcome with the tender x-ray RIXS beamline at PETRA-III [74]. In a study on Ca_2RuO_4, excitations at around 320 meV, 750 meV and 1000 meV were reported. However, the energy resolution at the ruthenium L_3-edge is currently well behind soft x-ray instruments and therefore no lower energy excitation or dispersive behaviour of the detected features could be unambiguously observed.

3.3 RIXS Study of $Ca_3Ru_2O_7$

Following the success of the previous RIXS studies on the single-layer Ca_2RuO_4, the question arises about how the interplay of the energy scales is affected by varying the effective dimensionality going from the single layer to the bilayer compound. Since both compounds undergo a similar c-axis compression but end up with different ground states, regarding both magnetical order and resistivity, a comparative study is most interesting. This section presents a combined oxygen K-edge XAS and RIXS study of $Ca_3Ru_2O_7$ and its comparison to Ca_2RuO_4 [47]. It shows how the difference in their magnetic ground states manifests in the excitation spectrum.

3.3.1 Methods

The floating zone technique was used to grow high-quality single crystals of $Ca_3Ru_2O_7$ [75, 76]. Before the experiment, the crystals were aligned ex situ using Laue diffraction and then cleaved in situ using the top-post technique, as described in section 2.1.2, to obtain full control over the crystal orientation and achieve a flat and clean surface. The XAS and RIXS measurements reported here were carried out at the ADRESS beamline of the Swiss Light Source (SLS) at the Paul Scherrer Institute in Switzerland [26]. At this beamline, the angle between the incident and scattered light is kept at 130°, fixing the modulus of the transferred momentum for a given photon energy. The in-plane momentum component, denoted as $\boldsymbol{q}_{\parallel} = (h \cdot 2\pi/a_T, k \cdot 2\pi/b_T)$, can be varied by controlling the angle θ between the incident light and the sample surface (ab-plane). The momentum transfer in this work was measured along the Ru–O bond direction, instead of the standard crystal lattice direction along the Ru–Ru bond. Therefore, the reciprocal space is indexed using the tetragonal convention along Ru–O with $a_T \approx b_T \approx \sqrt{a^2 + b^2}/2 = 3.86\,\text{Å}$ for $Ca_3Ru_2O_7$. Grazing and normal incidence refer to $\theta = 0°$ and $90°$, respectively. Linear vertical (LV, out of the scattering plane) and horizontal (LH, in the scattering plane) light polarizations were used and a total energy resolution at the oxygen K-edge of 53 meV (FWHM) was achieved. Spectra on $Ca_3Ru_2O_7$ were recorded at 20 K unless otherwise stated.

For the energy scale calibration of the spectra and the further analysis, the elastic scattering contribution, as well as the lowest lying excitation, are modelled by Gaussian lineshapes with widths set by the energy resolution. The second-lowest excitation is modelled by a response function of a damped harmonic oscillator (DHO) [30], and a quadratic function is used to describe the background.

The experimental setup for this study on $Ca_3Ru_2O_7$ is equivalent to that previously used for the study on Ca_2RuO_4 by L. Das *et al.* [72]. This and a comparable energy resolution, as well as similar experimental conditions, allow for the results on the two compounds to be directly compared.

3.3.2 Results

XAS and Orbital Selectivity at the Oxygen K-edge

Before discussing the XAS results and their interpretation on Ca_2RuO_4 and $Ca_3Ru_2O_7$, the choice of absorption edge and its advantages are further explained. It was mentioned above that direct ruthenium L_3-edge measurements have only recently become available and that their energy resolution is still very limited compared to soft x-ray measurements at the oxygen K-edge. In addition to the better energy resolution, measurements through the oxygen K-edge have the advantage of measuring orbitals selectively. In the absorption process, the electron is promoted from an oxygen $1s$ into a $2p_{x,y,z}$ orbital and the dipole matrix element for this transition is determined by the relative orientation of the polarization vector and the final state p orbital, since the initial s state is isotropic. In the setup employed here, the incident light beam is in the xz-plane with varying angle θ to the x-axis. For $\theta = 0$, the LH light polarization lies along the z-direction and interacts predominantly with oxygen p_z orbitals. Thus, the light polarization and incidence angle θ define which oxygen orbital is probed. In a second step, the each oxygen p orbital is hybridized with different ruthenium d orbitals, depending on the crystal site of the oxygen atom; see Fig. 3.5a. For example, the p_z orbital of an oxygen atom at the planar site hybridizes with d_{xz} and d_{yz} orbitals, whereas at the apical site, hybridization with the d_{z^2} orbital is enhanced. In this fashion, choosing the polarization and geometry allows for probing specific ruthenium d orbitals in the XAS and RIXS measurements. A summary of the different selection rules is presented in Table 3.1.

Figure 3.5b and c show the recorded XAS spectra for Ca_2RuO_4 and $Ca_3Ru_2O_7$ recorded with LH light polarization near grazing and normal incident light directions. At lower energies, the oxygen resonances hybridizing with the ruthenium t_{2g} states are probed. Additionally, the crystal-field environment and Coulomb interaction

		Apical O	Planar O
LH normal	p_x	$\boldsymbol{d_{xz}}$	$\boldsymbol{d_{xy}}$, $d_{x^2-y^2}$
LH grazing	p_z	d_{z^2}	$\boldsymbol{d_{xz}}$, $\boldsymbol{d_{yz}}$
LV	p_y	$\boldsymbol{d_{yz}}$	$\boldsymbol{d_{xy}}$, $d_{x^2-y^2}$

Table 3.1: Summary of the probed Ru d orbitals depending on polarization, experimental geometry and oxygen resonances. Orbitals written in bold correspond to the lower-lying t_{2g} states.

in tetragonal systems cause the apical edge to be lower in energy than the planar edge [77, 78]. Indeed, for the spectrum near normal incidence taken on Ca_2RuO_4, the first absorption peak is found at 529.1 eV, which can be assigned to the apical edge hybridized with the ruthenium d_{xz} orbital for this experimental geometry. If the angle is turned close to grazing incidence, the spectrum does not show a pronounced peak at this energy, which is expected since, at the apical site, there is only strong hybridization with the ruthenium e_g d_{z^2} orbital at higher energy. Instead, a strong peak is observed at 529.8 eV, which is the planar edge hybridized with ruthenium d_{xz} and d_{yz} orbitals for this geometry. Remarkably, the spectrum near normal incidence does not show a peak at this energy, which would correspond to hybridization with a ruthenium d_{xy} orbital. This is strong evidence for an almost fully occupied d_{xy} orbital that is inaccessible for absorption processes. This result is therefore in agreement with a crystal-field-driven insulating d_{xy} band.

For $Ca_3Ru_2O_7$, the oxygen sites are harder to distinguish, since there are three: the planar O(p), the interplanar O(ip) and the apical O(a); see Fig. 3.5. The planar and interplanar sites have similar crystal-field environments, as they both bond to two ruthenium atoms. Therefore, similarly to other layered oxides [77, 78], the first pre-edge at 528.3 eV is assigned to the apical resonance, whereas the second strong peak at 528.9 eV is assigned to the combined planar and interplanar resonances. It has to be noted that the reduced splitting of apical and planar resonances is known from the absorption study on the Sr sister series $Sr_{n+1}Ru_nO_{3n+1}$ [79, 80]. When going from single-layer to bilayer and trilayer compounds, apical and planar resonances move closer together, since their lattice sites become equivalent, as in the case of cubic $SrRuO_3$ [81]. Comparing the relative intensities of the apical and planar/interplanar resonances, it becomes apparent that the orbital occupation in $Ca_3Ru_2O_7$ is different from that in Ca_2RuO_4, with an only partially filled d_{xy} orbital. This also fits into the picture of a reduced c-axis lattice compression in $Ca_3Ru_2O_7$.

For both compounds, at higher energies, the resonances probing the oxygen p orbitals hybridized with the unoccupied ruthenium e_g states are observed. For the following RIXS measurements, the incident photon energy was tuned to the most intense planar/interplanar resonance at 528.9 eV.

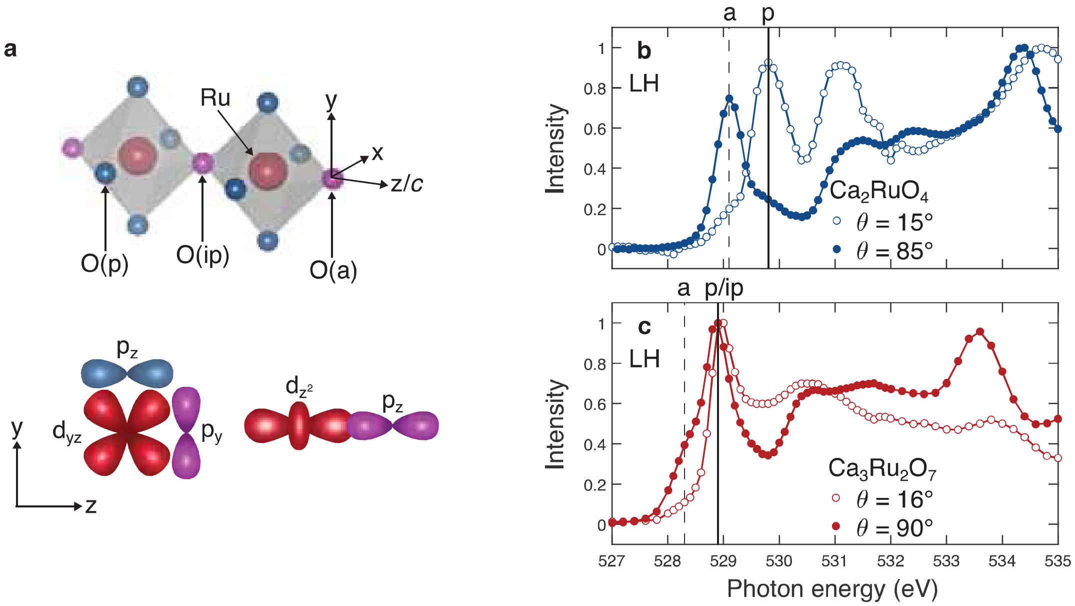

Figure 3.5: XAS measurements. **a** Simplified crystal structure showing two octahedra along the sample c-axis with illustrations of the oxygen p–ruthenium d hybridization. Atoms and orbitals corresponding to the planar and apical sites are shown in blue and purple, respectively. **b, c** XAS intensity measured as a function of incident photon energy on Ca_2RuO_4 and $Ca_3Ru_2O_7$, respectively. A background was subtracted and the data were normalized to the maximum value. The spectra were recorded with LH polarization with incidence angle as indicated. Dashed and solid vertical lines indicate apical and planar/interplanar oxygen resonances probing ruthenium t_{2g} states, respectively. Adapted from Ref. [47].

RIXS Excitation Spectra

Figure 3.6 shows an overview of the excitation spectra on $Ca_3Ru_2O_7$ compared to those on Ca_2RuO_4 [72], for different polarizations. The excitation spectrum of the semimetallic $Ca_3Ru_2O_7$ exhibits distinct differences from its band–Mott insulating sister compound. First, the dd excitation block at around 3.5 eV, originating in transitions between ruthenium t_{2g} and e_g levels, is shifted towards lower energies by ~ 0.5 eV. Second, the low-energy part shown in Fig. 3.6b reveals that two of the four low-energy excitations observed in Ca_2RuO_4 (labelled A, B, C and D) are completely absent in $Ca_3Ru_2O_7$. Among the two excitations present in $Ca_3Ru_2O_7$, A and B, the B excitation is considerably broadened and shows an extended tail towards higher energies, hinting at possible low-intensity excitations at higher energy loss; see also Fig. 3.7a.

To extract information about the lowest-energy excitation A in $Ca_3Ru_2O_7$, a careful analysis is required, since it overlaps partially with the elastic scattering peak. The previously described fitting procedure with components for elastic scattering, A

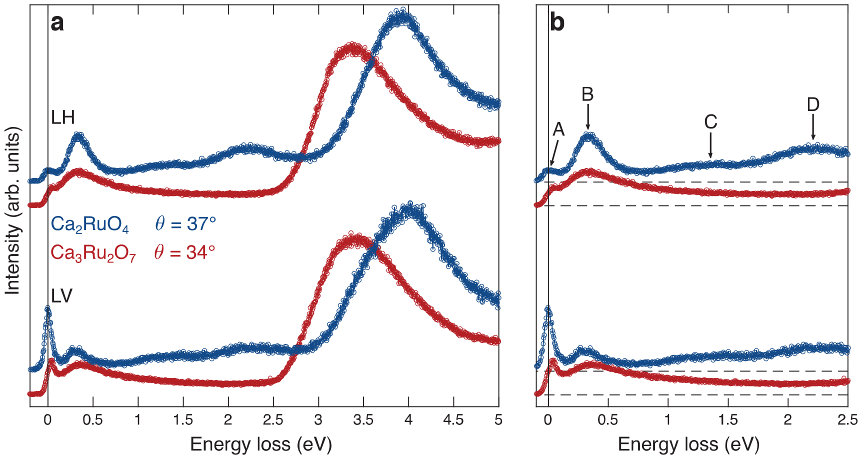

Figure 3.6: RIXS spectra. **a** Full RIXS spectra for both Ca_2RuO_4 and $Ca_3Ru_2O_7$ recorded with LH and LV polarized light as indicated. **b** Expanded view of **a** on the low-energy part of the spectrum featuring excitations A, B, C and D. Adapted from Ref. [47].

excitation, B excitation and background allow for an extraction of the spectral weight of the A excitation; see Fig. 3.7b. For incident light close to the specular condition, the elastic peak is the most pronounced and the A excitation is only visible as a shoulder on the higher energy loss side. In contrast, when θ is lowered and one moves further away from the specular condition, elastic scattering is suppressed and is only visible as a shoulder on the lower energy loss side of the now-pronounced A excitation. The fitting procedure also allows for the subtraction of elastic, B excitation and background contributions, which provides a clear picture of the momentum evolution of the A excitation; see Fig. 3.7c. At 20 K, the peak position of the A excitation moves towards lower energies upon increasing the in-plane momentum transfer h. It can also be seen that the A excitation and its dispersion are detectable at least up to 80 K, which is well above the magnetic and structural transition temperatures of $Ca_3Ru_2O_7$.

The momentum dependence of the A and B excitations in $Ca_3Ru_2O_7$ is compared to the corresponding excitations in Ca_2RuO_4 in Fig. 3.8. For the A excitation in $Ca_3Ru_2O_7$, the peak position from fitting is shown, whereas for the B excitation, the maximum obtained from the derivative of the spectrum is depicted, since the peak is very broad. The dispersions reveal fundamental differences between the low-energy excitations in Ca_2RuO_4 and $Ca_3Ru_2O_7$. Whereas a slight upward dispersion could be detected for the B excitation in Ca_2RuO_4, the broadness of this excitation in $Ca_3Ru_2O_7$ and the resulting large error bars allow no clear dispersion to be observed for this compound. In contrast, the A excitation did not show a measurable dispersion in Ca_2RuO_4 with the applied energy resolution, whereas a fast dispersion to lower

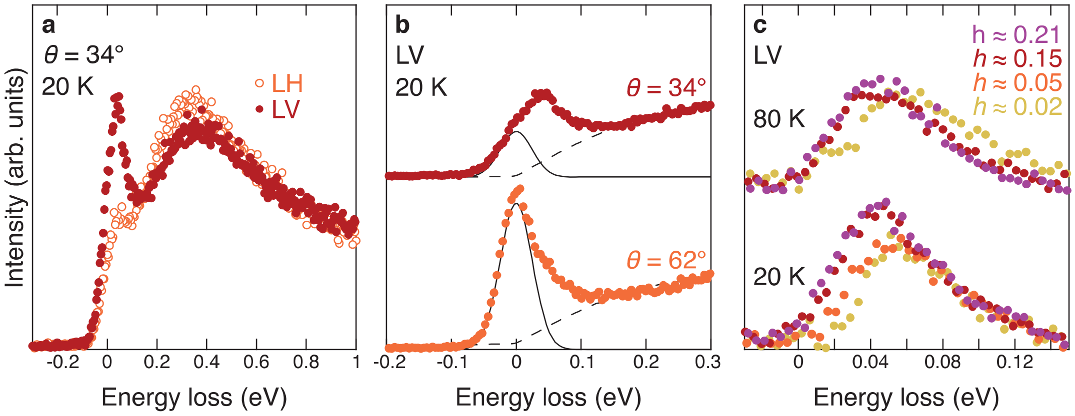

Figure 3.7: A excitation of $Ca_3Ru_2O_7$. **a** Spectra recorded with different polarizations. **b** Spectra recorded at different incidence angles. Solid black lines are Gaussian fits to model the elastic scattering. Dashed black lines are DHO + background fits to model the B excitation. **c** Spectra with elastic scattering, B excitation and background subtracted to show the dispersion of the A excitation for temperature and in-plane momentum transfer h as indicated. Adapted from Ref. [47].

energies is detected in $Ca_3Ru_2O_7$. As a comparison, the reproduced dispersion of a phonon mode at comparable energy in Sr_2RuO_4 is shown, measured by neutron scattering [82]. The A excitation disperses much faster than what is expected from a phonon mode, suggesting a different origin. Another difference between the two compounds is the overall energy of the A excitation. In $Ca_3Ru_2O_7$, it is at significantly lower energies of around 55 meV, as opposed to around 80 meV in Ca_2RuO_4.

3.3.3 Interpretation and Discussion

The results on the excitation spectrum of $Ca_3Ru_2O_7$ compared to Ca_2RuO_4 wonderfully show how the difference in ground states is imprinted on the low-energy excitation sector. The difference in the local dimensionality around the ruthenium atoms greatly influences the level splitting set by Hund's coupling, crystal-field splitting and spin–orbit coupling, and leads to a distinctly different set of low-energy excitations. The previously discussed C and D excitations in Ca_2RuO_4 are associated with intra-atomic singlet–triplet excitations set by the Hund's coupling and Coulomb interaction; see section 3.2. Exactly these two energy scales are responsible for the Mott insulating ground state in Ca_2RuO_4. In $Ca_3Ru_2O_7$, on the other hand, the C and D excitations are completely absent, which is in accordance with the semimetallic ground state.

At lower energies, the A and B excitations are present for both compounds, although they display several differences in excitation energy and dispersion behaviour. To

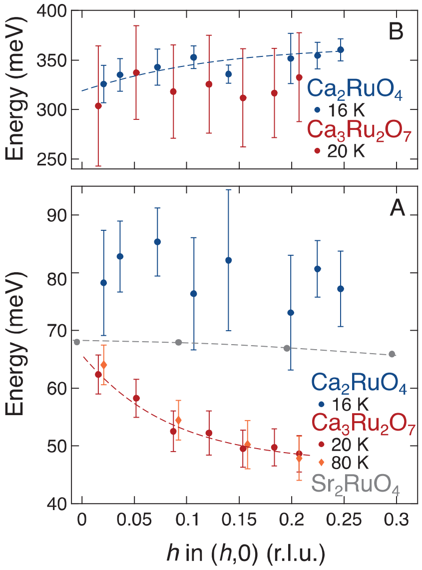

Figure 3.8: Dispersion of A and B excitations. Excitation peak position as a function of in-plane momentum transfer h for the A (bottom) and B (top) excitations. In $Ca_3Ru_2O_7$, error bars on the A excitation indicate a standard deviation 3σ from the fitting, while on the B excitation, the error bars indicate the peak width at 98% of the total height. Grey data reproduce the phonon dispersion in Sr_2RuO_4 measured with neutron scattering [82]. Dashed lines are guides to the eye. Adapted from Ref. [47].

gain insight into the different nature of these excitations, the RIXS response was calculated for both compounds following the method described in Ref. [72]. A model Hamiltonian is defined on a cluster consisting of two in-plane ruthenium atoms connected via a planar oxygen. The model allows for the bond bending due to the rotation of the octohedra around the c-axis. The model Hamiltonian is composed of the following terms [83, 84]:

$$H = H_{\text{kin}} + H_{\text{el–el}} + H_{\text{cf}} + H_{\text{soc}} + H_{\text{m}} \tag{3.1}$$

where H_{kin} describes the kinetic operator of the ruthenium–oxygen connectivity and $H_{\text{el–el}}$ is the Coulomb interaction U, including intra- and interorbital terms, the Hund's coupling J_H and the pair-hopping term. H_{cf} describes the crystal-field potential Δ due to the compression of the RuO_6 octahedra along the c-axis, H_{soc} is the spin–orbit coupling λ term of the Hamiltonian. Lastly, H_{m} describes an effective exchange field to account for the different magnetic ground state in $Ca_3Ru_2O_7$, in which the magnetization at the ruthenium site is ordered ferromagnetically in the plane (A-type AFM). On the ruthenium site, the Hamiltonian acts within the t_{2g} subspace. The RIXS response is then inferred via exact diagonalization of the Hamiltonian to calculate the cross section of an excitation and subsequent relaxation of an electron from an oxygen $1s$ to $2p$ state within the fast collision

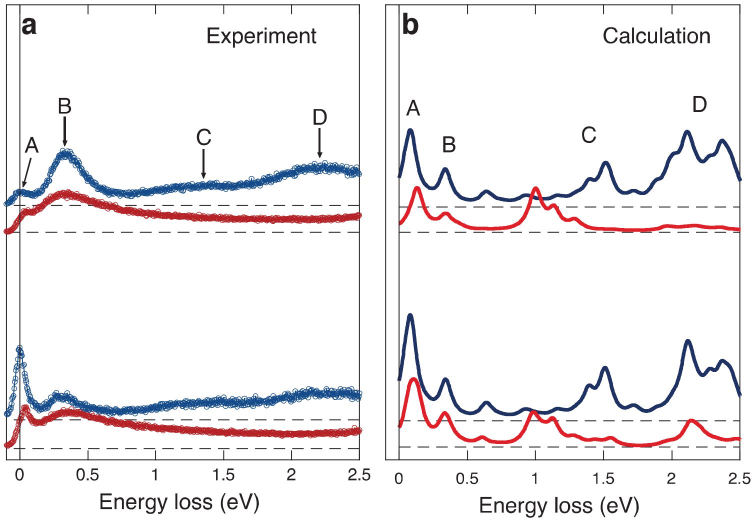

Figure 3.9: Experiment and Calculation. **a** Measured RIXS spectra from Fig. 3.6. **b** Corresponding calculated RIXS spectra of Ca_2RuO_4 and $Ca_3Ru_2O_7$. Adapted from Ref. [47].

approximation [13, 85].

The calculated RIXS spectra of Ca_2RuO_4 and $Ca_3Ru_2O_7$ are compared to the measured spectra in Fig. 3.9. Overall, a good agreement between experiment and calculation is observed. The four excitations in Ca_2RuO_4 are reproduced in a similar energy range and it can be seen that the intensity for $Ca_3Ru_2O_7$ is reduced, especially above 1 eV, which is in agreement with the absent C and D excitations. However, the suppression is more pronounced in the experimental data, which may be due to the fact that $Ca_3Ru_2O_7$ is less insulating and the cluster calculation may not be able to account for the more delocalized nature. However, this comparison allows for a refined set of values for the energy scales: $U = 2.0\,\mathrm{eV}$, $J_H = 0.4\,\mathrm{eV}$, $\Delta = 0.3\,\mathrm{eV}$ and $\lambda = 0.05\,\mathrm{eV}$. These values are comparable to what has been used in dynamical mean-field theory calculations [16] and in modelling spin-excitation dispersion [60, 72].

Considering the lower A and B excitation in Ca_2RuO_4, they have been assigned to composite spin–orbital excitations determined by the relative strength of the crystal-field splitting and spin–orbit coupling [72]. In $Ca_3Ru_2O_7$, excitations at similar energy scales are observed and therefore the possible spin–orbital/magnetic origin is discussed here, especially for the lowest-lying A excitation.

Before diving into this discussion, it has to be noted that the A excitation has an energy scale that is typical for both magnons and optical phonons. However, as explained above, the strong dispersion of this excitation, especially near the zone centre is highly atypical for optical phonons; see Fig. 3.8 for the case of Sr_2RuO_4 [82].

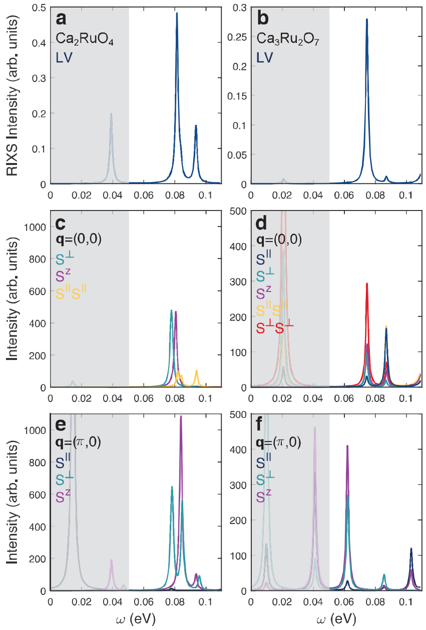

Figure 3.10: Spin structure factors. **a, b** Calculated RIXS spectrum focusing on low energies. **c-f** Dynamic spin structure factors $S^{\mu}(\boldsymbol{q}, \omega)$, spin–spin dynamic spin structure factors $(S_i \cdot S_{i+1})^{\mu}(\boldsymbol{q}, \omega)$ for $\mu = \parallel, \perp, z$, and for $\boldsymbol{q} = (0,0)$ and $(\pi, 0)$ as indicated. The grey shaded area illustrates the region inaccessible at the time of the study due to limited resolution. Adapted from Ref. [47].

Another indication against a phononic nature for the A excitation is the fact that optical phonons in this energy region stem from vibrations of the apical oxygen, but here the excitation is probed via the planar/interplanar resonance. Hence, the assignment of a magnetic origin for the A excitation in $Ca_3Ru_2O_7$ seems more appropriate. The fact that the excitation is observed even at 80 K, above the magnetic ordering transition, is not unusual, due to the persistence of short-range magnetic correlations. This has been observed for paramagnon excitations in cuprates and iron pnictides [30, 86, 87].

To understand the detailed mechanism of the magnetic origin of the A excitation, the dynamic spin structure factors $S^{\mu}(\boldsymbol{q}, \omega)$ and the spin–spin dynamic spin structure factors $(S_i \cdot S_{i+1})^{\mu}(\boldsymbol{q}, \omega)$ for $\mu = \parallel, \perp, z$ have been calculated; see Fig. 3.10. Since the magnetic ground state is made by moments aligned in the ruthenium plane, $\parallel$, $\perp$, z refer to spin mode excitations that are collinear, perpendicular in-plane and perpendicular out-of-plane with respect to the ground state magnetic moment orientation, respectively; see inset of Fig. 3.2. For the cluster adopted in the calculation, the only accessible momenta are $\boldsymbol{q} = (0,0)$ and $(\pi, 0)$, which are displayed in the figure. For Ca_2RuO_4 in the left panels, the A excitation at $\boldsymbol{q} = (0,0)$ can be